Development of Nanotemplates and Nanomagnetic Materials for Data Storage Applications

A Dissertation

Presented to

the Faculty of the Materials Science and Engineering Program

University of Houston

In Partial Fulfillment

of the Requirements for the Degree

Doctor of Philosophy

in Materials Science and Engineering

by

Dahye Lee

August 2016

Development of Nanomaterials and Nanomagnetic Materials for Data Storage Applications

Dahye Lee

Approved:

Chair of the Committee
Dr. Dmitri Litvinov, Professor
Materials Science and Engineering
Electrical and Computer Engineering

Committee Members:

Dr. T. Randall Lee, Professor
Chemistry

Dr. Paul Ruchhoeft, Associate Professor
Materials Science and Engineering

Dr. Richard Willson, Professor
Chemical and Biomolecular Engineering

Dr. Karen Martirosyan, Professor
Physics
University of Texas at Rio Grande Valley

Dr. Suresh K. Khator, Associate Dean
Cullen College of Engineering

Dr. Dmitri Litvinov, Professor and Director
Materials Science and Engineering

Acknowledgment

I would like to thank my two advisors, Dr. Dmitri Litvinov and Dr. T. Randall Lee for the knowledge of chemistry and engineering they helped me build. My sincere thanks to Dr. Litvinov who taught me how to swim in the engineering sea and provided access to equipment and the scientific environment so I could enjoy the engineering sea life and grow independently. I am honored to know Dr. T. Randall Lee who is my advisor as well as my mentor in all things. He cares about his students like his own kids and helps us to grow to be better scientists by sharing his extensive knowledge and substantial emotional support. Thanks to Dr. Paul Ruchhoeft, who was willing to share his knowledge and Dr. Richard Willson for being in my committee, for which I am honored. Also, I thank Dr. Karen Martirosyan who has been a great supporter at UT RGV whenever I visited to do magnetic research.

I owe a lot to my colleagues in chemistry and engineering groups. Especially Dr. Long Chang who trained me to use different equipment, gave me the skills to become a good engineer, and Ivan Nekrashevich, with whom I can always have a worthy and productive discussion on physic theories and chemistry. Thanks to Mary Nguyen, who is like my big sister in the cleanroom, supporting me with amazing food and counseling me about life. Many thanks to my friends all over the world who have been with me through the good and the bad, and my Grandparents who are always looking after me in heaven. Last, but certainly not least, the most important people in my life; my amazing parents and sister. They have provided me the opportunity to get a great education and improve the quality of my life. They have instilled in me a deep sense of pride in productivity that has served me well.

Development of Nanotemplates and Nanomagnetic Materials for Data Storage Applications

An Abstract

of a

Dissertation

Presented to

the Faculty of the Materials Science and Engineering Program

University of Houston

In Partial Fulfillment

of the Requirements for the Degree

Doctor of Philosophy

in Materials Science and Engineering

By

Dahye Lee

August 2016

Abstract

Materials engineered on the nanoscale level currently draw much attention due to the variety of applications derived not only from their minimized size, but also from the unique physical properties that set them apart from bulk materials. Historically, the nanoscale has been used for over a hundred years. However, with the currently available instruments, scientists now have the capabilities to observe what is happening at the nanoscale. This enables a better understanding that leads to improved design and control of nanoscale materials, ultimately leading to new applications. Particularly, research and development of magnetic devices for data storage applications has made significant technological impacts for the past four decades. Our society has greatly benefited from the significant downsizing and increased performance of data storage technology. To improve data storage technology further, there are two approaches: (1) develop new materials or (2) determine improved processes to utilize known materials.

In this study, a new fabrication process for generating nanoscale patterns in polymers is explored (Chapter 2 and 3), and a new magnetic material is developed by the functionalization of graphene (Chapter 4). The fabrication process can produce 40 nm openings of hexagonal in a polymer, which can be used as a mask to pattern other materials or as molds for filling other materials inside. This patterning technique might enable a more advanced magnetic recording technology, bit-patterned-media (BPM). The chemically functionalized graphene with sulfates and oxygens were investigated for potential applications in spintronics.

Table of Contents

List of Figures

List of Tables

Chapter 1. Introduction to Magnetic Recording

1.1 History of Magnetic Recording

In 1956, IBM commercialized the first hard disk drive (HDD), called the 350 disk storage, which was a major component of the 305 RAMAC (Random Access Memory Accounting) [1]. As you can see in Figure 1.1, the 350 disk storage weighs more than a ton and occupied a space 60 inches long, 68 inches high and 29 inches deep [1]. This drive could store 5 megabytes (10^6 bytes) of data and cost $10,000,000 per gigabyte [1]. In 2016, a HDD weighs 1.72 pounds and can be held in one hand (4 × 5.8 × 0.6 in) [2]. A modern HDD can store 8 terabytes (10^{12}) at a cost of $0.03 per gigabyte. Since its invention, the HDD has become approximately 8,500 times smaller, 1,000 times lighter, and 100 million times cheaper.

Figure 1.1 The first HDD by IBM in 1956 compared to a HDD in 2010 [1].

The storage capacity for HDDs has grown since consumers demand more data storage capacity in a smaller, lighter, and more affordable package. The industry has

satisfied consumer demands by increasing the areal density and number of bits per square inch of the HDD every year. Figure 1.2 shows the areal density of HDDs since the 1980s. Since 1992, the areal density has been increasing by approximately 60–100% every year. The growth began to slow down in 2005, and it will continue to slow as HDD technology approaches the limit of the technology. The limitations of HDD technology are well understood, and the only options toward overcoming the limit is by developing new technologies or/and materials. One contending technology that can enable a healthy areal density growth rate is called bit-patterned media, BPM.

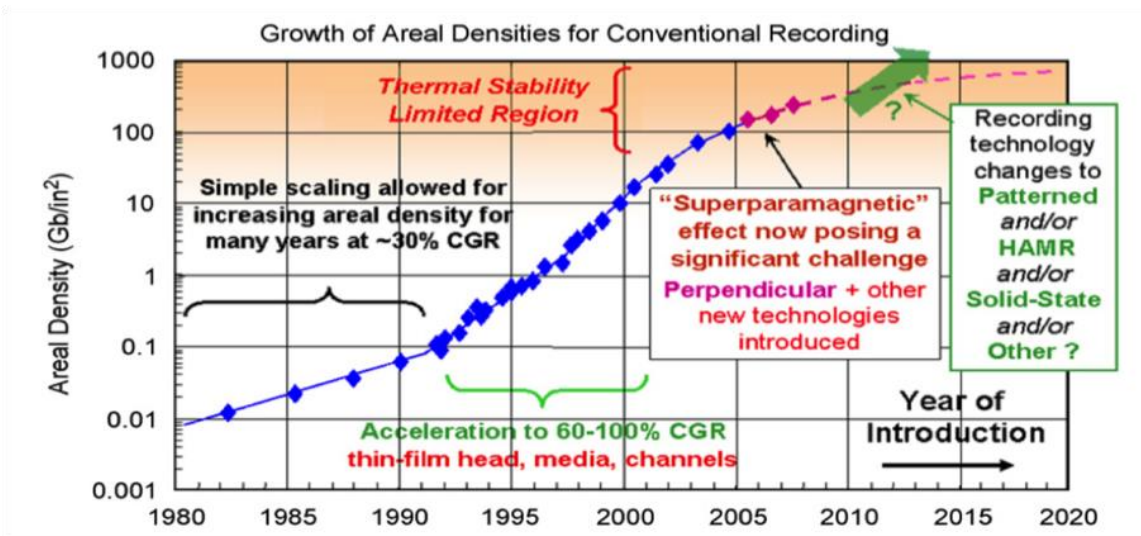

Figure 1.2 Growth of areal density over time [3].

1.2 Magnetic Recording

Magnetic materials are composed of grain, and each grain aligns with respect to their easy axes. Shown in Figure 1.3 is a representation of 2 bits of data. The left group consists of a number of grains that are magnetized approximately to the right. Similarly,

the right group consists of a number of grains that are magnetized approximately to the left. A typical hard disk contains billions of such groups, where the magnetization of each group points approximately left or right.

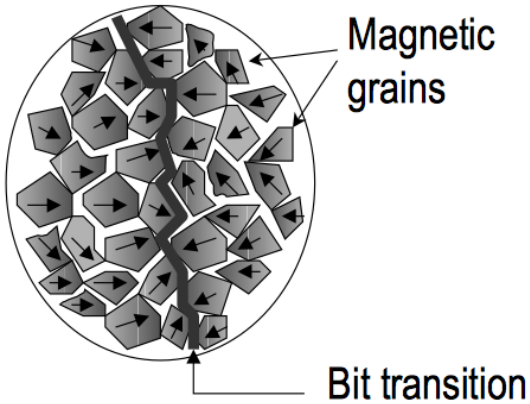

Figure 1.3 Schematic of grains and bits [4].

In magnetic recording, information is stored in the magnetization direction of a magnetic grain. A group of grains that are magnetized approximately in the same direction represents a single data bit. Each bit can have one of two opposite states: either magnetized left or magnetized right. Thus, in a HDD, data are stored in the magnetization directions of nanomagnets.

1.3 Conventional Longitudinal and Current Perpendicular Magnetic Recording

Longitudinal magnetic recording systems were used since the mid 1980s until the mid 2000s. The read/write head produces a strong magnetic field to orient the bits

along a track, as shown in Figure 1.4. The orientations of the bits are read by giant magnetoresistive (GMR) sensors and the HDD translates the readings into computer data.

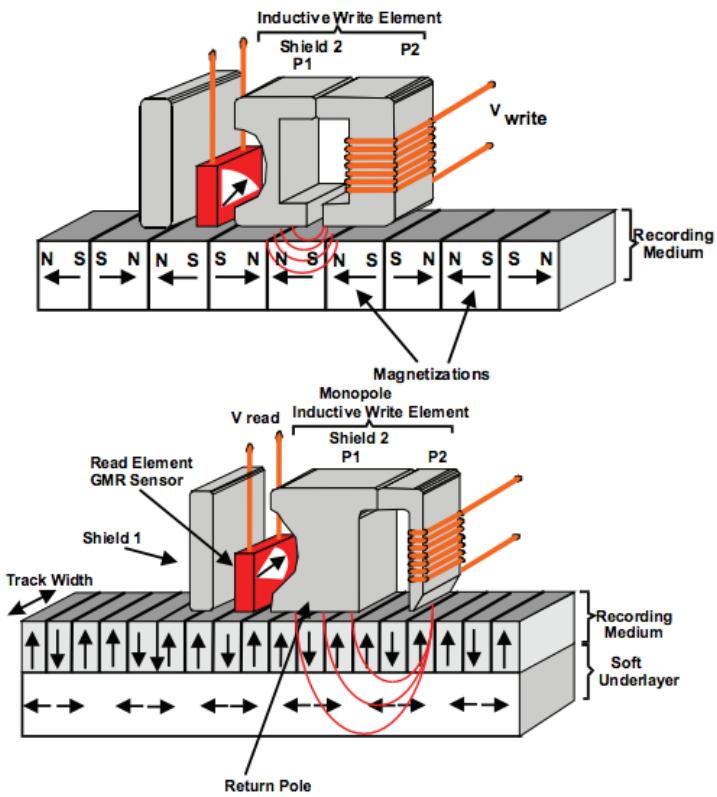

Figure 1.4 Schematic of longitudinal and perpendicular recording system [5].

It is necessary to have approximately 50–100 grains per bit in order to achieve a reasonable signal-to-noise ratio. The signal-to-noise ratio can be approximated by the following equations:

$$\text{SNR} \sim \log(N) \text{ and} \tag{1.1}$$

$$\text{Grain size} \sim \frac{1}{\sqrt{areal\ density}}\,. \tag{1.2}$$

In equation 1.1, SNR is the signal-to-noise ratio and N is the number of grains. For example, we can imagine a bit that consists of either 100 grains or 10 grains. In the case where one bit consists of 100 grains, if 5 grains are unstable and demagnetize (noise), the net magnetization (signal) is still 95 grains. In this situation, the reader can reliably identify the magnetization of the bit. However, when a bit consists of 10 grains and 5 grains are demagnetized, then the average orientation of the bit is neither left nor right, and there is no way for the reader to make a determination. In this case, the reader has to guess the magnetization of the bit, and there is a 50% chance to be wrong, leading to corruption of the data. It is not guaranteed that all the grains are stable, so we need many grains per bit in order to achieve sufficient reliability.

On the other hand, in order to increase the areal density, the size of each bit must be made smaller. This can be achieved by making the grains smaller or reducing the number of grains per bit. Smaller grains are less stable, and fewer grains per bit are less reliable. Engineers have been pushing both fronts toward their absolute limit. When the grains are made too small, they become thermally unstable. This situation called the superparamagnetic limit. At the superparamagnetic limit, data storage is no longer physically possible, and it is predicted to occur at an areal density of approximately 200 gigabits per square inch for longitudinal recording technology.

In 2005, perpendicular recording technology was introduced as longitudinal technology was struggling with the superparamagnetic limit. In perpendicular technology, the bits are aligned perpendicular to the surface of the disk. This new technology enables higher areal density compared to longitudinal recording. Perpendicular recording technology achieves more stability in many ways. The adjacent

bits mutually stabilize each as opposed to longitudinal recording where adjacent bits repel each other. The benefits of perpendicular magnetic recording technology permits engineers to increase areal density further at a healthy rate. However, it is predicted that perpendicular recording will encounter the superparamagnetic limit at an areal density of 500–1000 gigabyte/in^2 [6, 7].

1.4 Fundamental Limit: Superparamagnetism

Once a ferromagnetic material is magnetized, it remains magnetized for a long time. However, when the volume of the magnet becomes sufficiently small, they begin to switch back and forth so quickly that their net magnetic moment is zero. This situation corresponds to the superparamagnetic limit, and data that are recorded on a small timescale are not useful. When the magnetic grains become smaller than the superparamagnetic limit, they switch erratically at room temperature [8]. The mean time between the two states of spontaneous magnetization reversal of a magnetic grain is

$$t = \frac{1}{f_0} \exp\left(\frac{K_u V}{k_B T}\right) , \tag{1.3}$$

where t is the switching time, f_0 is the attempt frequency, K_u is the magnetic anisotropy of the grain, V is its volume, k_B is the Boltzmann constant, and T is the temperature. When engineering a hard drive, it is typical to set the switching time to approximately ten years and engineer materials to achieve the appropriate performance. Thus Equation 1.3 can be simplified to

$$\frac{K_u V}{k_B T} > 60 - 80 \tag{1.4}$$

in the case where reliable stable data storage is achieved for 10 years [9]. The parameters that engineers can control are V and $K_{u,}$ since k_B is a constant, and the hard drive will be operating at approximately room temperature.

1.5 Future Magnetic Recording

A new technology is required to supersede perpendicular recording as it approaches the superaparamagnetic limit. Several approaches have been suggested such as heat assisted magnetic recording (HAMR) [10–12], shingled magnetic recording (SMR) [13] and bit-patterned media (BPM) [9, 14]. In this work, we investigate an approach toward realizing BPM.

1.6 Bit-Patterned Media (as Future Magnetic Recording)

BPM is a drastic change to magnetic recording, and it is illustrated in Figure 1.5. Longitudinal and perpendicular recording uses granular media or continuous media so that there is no clear-cut-boundary between bits. On the other hand, patterned media uses discrete bits. BPM stores data on a single large magnetic grain per bit instead of 100 small grains per bit. This strategy enables BPM to achieve much higher bit densities than perpendicular recording technology [15].

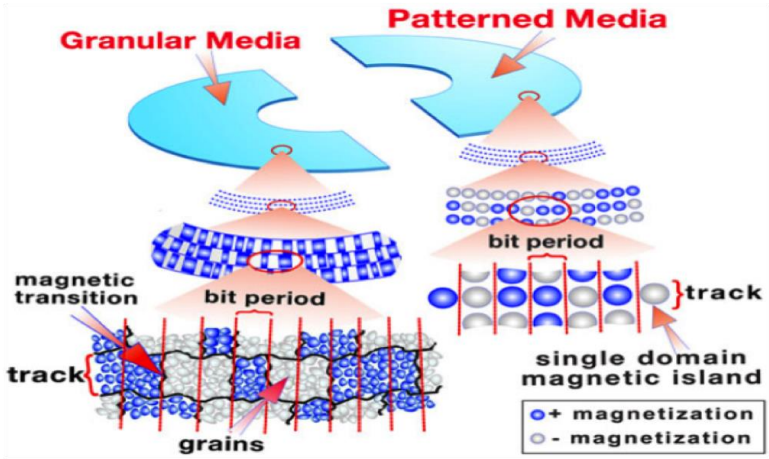

Figure 1.5 The comparison of conventional versus patterned media [16].

1.7 Potential Data Storage Applications with Graphene-Based Materials

The spin of the electron was not used in mainstream charge-based electronics until the early 2000s. A new technology, spintronics, has emerged with the introduction of electron spin that carries information; this technology has opened opportunities for the generation of new devices. Among the advantages of new spintronics-based devices compared to the conventional semiconductor-based devise are the increased data processing speed and decreased power consumption [17].

Graphene has been suggested as one of the potential materials for spintronic applications. It possesses a weak spin-orbital coupling, which enables a long spin diffusion length and low hyperfine interactions between the nucleus and the electron spin compared to some conventional semiconductors due to the zero nuclear spin of the most abundant carbon isotope, ^{12}C [18–20]. In addition, graphene and its most common derivatives, graphene oxide, are flexible and easily fabricated [21]. The combination of

weak spin-orbit coupling and low hyperfine interaction strength leads to an increase in the coherence time of the spin states in graphene [18, 22]. This makes graphene a material of interest for spintronics, information storage, high speed computing, communications, and low-power-consumption electronics [17, 23–25]. However, as of now, studies of magnetism in graphene are limited and are not easily accessible due to the fact that the magnetic signals produced by graphene samples are typically weak. Conventional methods of fabrication of graphene and its functionalization rely on the use of substrates that allow production of only small quantities of a material, which further complicates studies magnetism-related studies of graphene. In this dissertation, we explore the use of oxidized graphene sheets, which are free floating in water. This approach allows us to study relatively large quantities of the material and enables chemical modification and characterization of the magnetic properties.

Chapter 2. Fabrication of Nanopatterns by Electron-Beam Lithography

2.1 Motivation

Bit patterned media can support higher areal densities than continuous media. Bit patterned media achieves higher stability by lithographically defining discrete isolated bits consisting of a single large magnetic. Lithography can easily produce small circularly patterns, but non-circular patterns might improve the stability of magnetic bits. In this chapter, we investigate a process to fabricate non-circular patterns via e-beam lithography. In Chapter 3, we investigate a higher throughput approach toward making non-circular patterns by processing block copolymers.

2.2 Previous Work in Our Laboratory

Our laboratory developed a new fabrication technique that enables close-packed non-circular patterns to be produced over large areas with low cost, as shown in Figure 2.1.

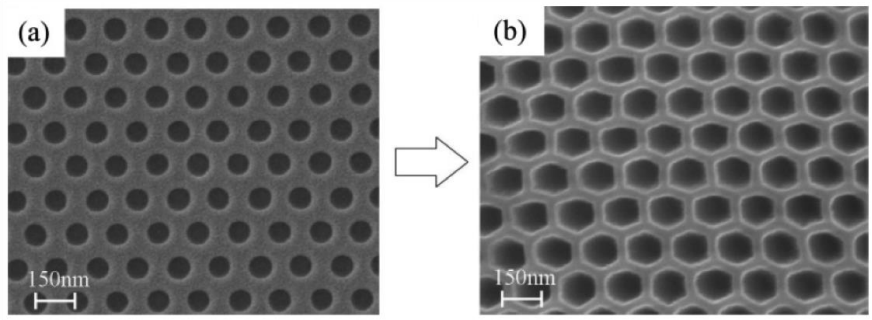

Figure 2.1 (a) An SEM image of 85 nm openings on PMMA using e-beam lithography. (b) Top view of 105 nm hexagonal openings on a 150 nm pitch after 12 min of self-limiting Ar^+ milling at a beam energy or 500 eV [26].

The circular opening patterns were fabricated by e-beam lithography and then further processed in an Ar^+ mill to obtain non-circular patterns. It is difficult to get the non-circular patterns directly through electron beam lithography because of the proximity effect and limitations in resist resolution. However, by subjecting the patterns to a low energy dry etching process, the array of circles are transformed into an array of hexagons, as shown in Figure 2.1. For this investigation, polymethyl methacrylate (PMMA) was used as a positive tone resist to fabricate the circular patterns. When the pattern is processed in a low energy argon mill, the patterns expand, but the pattern spacing remains the same. The larger pattern area produces a larger bit volume, which is theoretically more stable. Therefore, this approach may be better than BPM that uses circular bits. To improve upon the previous work, we investigate the feasibility of fabricating smaller patterns. PS-PMMA block copolymer (BCP) is an interesting alternative patterning method to e-beam lithography because of its high throughput. It has been shown that He beam irradiation can selectively remove PMMA from PS-PMMA, which produces PS patterns with cylinder shaped pores instead of PMMA. Therefore, unlike from the previous work with PMMA, we needed to transform the circular patterns to non-circular patterns in PS. In this chapter, we investigate the feasibility of using low energy argon milling to transform circular patterns in PS into non-circular patterns.

2.3 Experimental Procedure

Polystyrene (PS) powders with a 10,500 g/mol PS (Mw/Mn=1.06) and 2,000 g/mol PS (Mw/Mn=1.10) were purchased from Polymer Source and Alfa Aesar, respectively.

The PS powder was dissolved in toluene, a commonly used solvent for PS [27], for 2 days with stirring to make 2.8 % concentration by weight inside an amber vial. The solution was filtered by 0.2 μm pore size PTFE filter with a glass syringe (VWR, Poulten and GrafFortuna™ Glass Syringes, Air-Tite, 100ml) twice into the same vial to remove particulates. The PS solution was then spun onto a substrate that consists of Si/SiO_2 (500 nm)/Ta (30 nm). The Ta metal layer was used to improve imaging in a scanning electron microscope. The Ta layer was sputtered onto an oxide wafer via an ultra-high-vacuum sputtering system. Spin coating was used to coat PS on the wafer. It was observed that using less than 2000 rpm produces a non-uniform thickness over the wafer. In this experiment, the spin coater was programmed to spin at 2500 rpm for 60 seconds with an acceleration of 1250 rpm/s. The layout pattern was designed in K-layout and e-beam lithography was used to write the patterns on the resist. Then it is developed by immersion in toluene, tetrahydrofuran (THF), or *p*-xylene for 45 sec and rinsed with isopropanol (IPA) for 10 sec. The shape of the patterned PS was determined by SEM, and the thickness and roughness was determined by AFM. Finally, Ar^+ milling was used to transform the circular to non-circular patterns.

2.4 Electron-Beam Lithography

2.4.1 Parameter 1: Developer

The e-beam lithography system (JEOL JBX 5500FS eBeam writer) was used to fabricate patterns in PS. This system produces a 50 kV electron beam from a ZrO/W emitter and has a four-stage e-beam focusing lens system. The electron beam system

scans a 4 nm wide gaussian beam using a 12 Mhz vector scanner with a resolution of 0.5 nm [28].

The first step toward printing good patterns is to determine the critical dose. The critical dose is determined by performing a dose series and analyzing the contrast curve. Figure 2.2 shows a typical contrast curve where D_0 and D_{100} are the intersections of a line that has the highest slope that intersects at zero and full resist thickness, respectively. The contrast [28] can be calculated by

$$\gamma = (log\frac{D_{100}}{D_0})^{-1}. \quad \textbf{(2.1)}$$

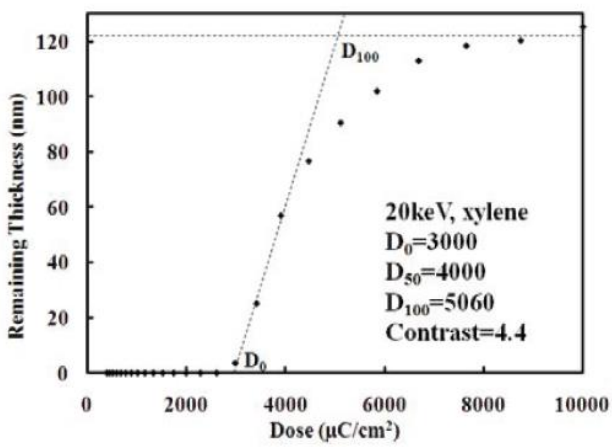

Figure 2.2 Contrast curve for polystyrene exposed at 20 keV and developed by (o-, m-, p-mixed) xylene for 90 s at room temperature [29].

The contrast curve for PS developed in various developers is shown in Figure 2.3. A dose around 2,500 μC/cm^2 is the critical dose to fabricate the patterns with 10,500 g/mol PS for the three developers used. To explain the contrast curve, at a dose of 2,000 μC/cm^2 and below, the PS will be completely dissolved in development process. At a

dose above 2,500 μC/cm^2, the PS will not be dissolved by the developer and will remain on the sample. This classifies PS as a negative-tone resist, where e-beam exposure induces crosslinking, which makes the PS insoluble in a developer.

In this study, toluene, THF, and p-xylene were used as developers. The dose series with these three developers are shown in Figure 2.3. THF and p-xylene appear to be better developers than toluene because they have better contrast; however, THF soaks up moisture leading to challenges with regard to reproducibility.

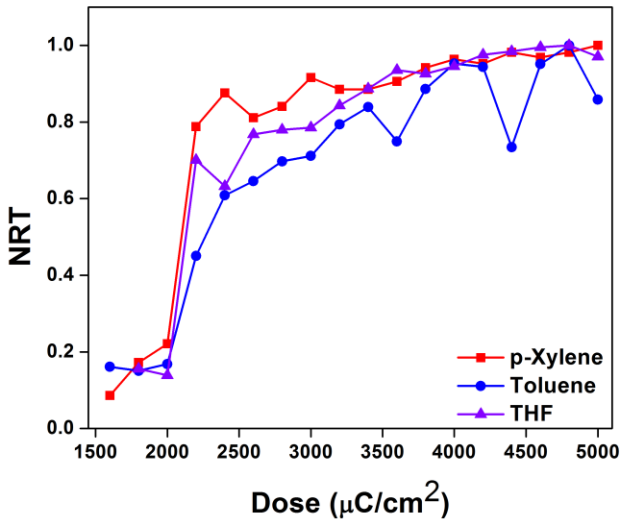

Figure 2.3 Does series of 10,500 g/mol PS with different developers; toluene, THF, and *p*-xylene were plotted as normalized remaining resist thickness (NRT) versus does (μC/cm^2).

Various doses and various widths of square patterns were tested with each of the three developers. Figure 2.4 and 2.5 show the SEM images of the results: (A) toluene, (B) THF, and (C) *p*-xylene with (a) 20 nm, (b) 60 nm, (c) 80 nm, and (d) 100 nm width of squares. Toluene and *p*-xylene were tested from 800 to 2400 μC/cm^2 at intervals of 200 μC/cm^2, and THF was tested from 1400 to 2200 μC/cm^2 with intervals of 100 μC/cm^2.

Higher dosages produce higher contrast in an SEM, and some of low dosages were difficult to observe.

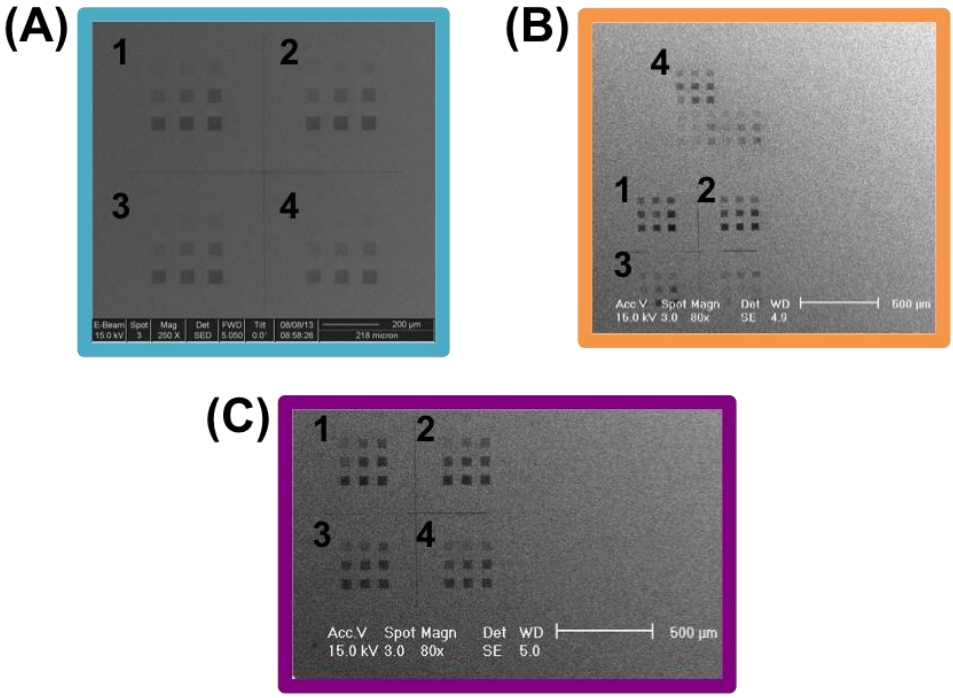

Figure 2.4 Dose and size test with (A) toluene, (B) THF, and (C) *p*-xylene as developers. The pattern contains sets of (1) 20 nm, (2) 60 nm, (3) 80 nm, and (4) 100 nm wide squares. Each set is exposed at 9 different dosages.

As shown in Figure 2.5 (A), patterns smaller than 60 nm are difficult to fabricate with toluene. Over-dosing, for example d_2200 of Figure 2.5 (A), produces smaller than expected patterns compared to the intended designed shape; on the other hand, under-dosing, as in d_1400, makes the patterns dull without having sharp edges between patterns. As seen in Figure 2.5 (B) and (C), THF and p-xylene can produce smaller and sharper patterns than toluene. However, THF is hygroscopic, and the reproducibility is consequently low. Thus, p-xylene is the best developer for this process and is the only developer used for the rest of the investigation.

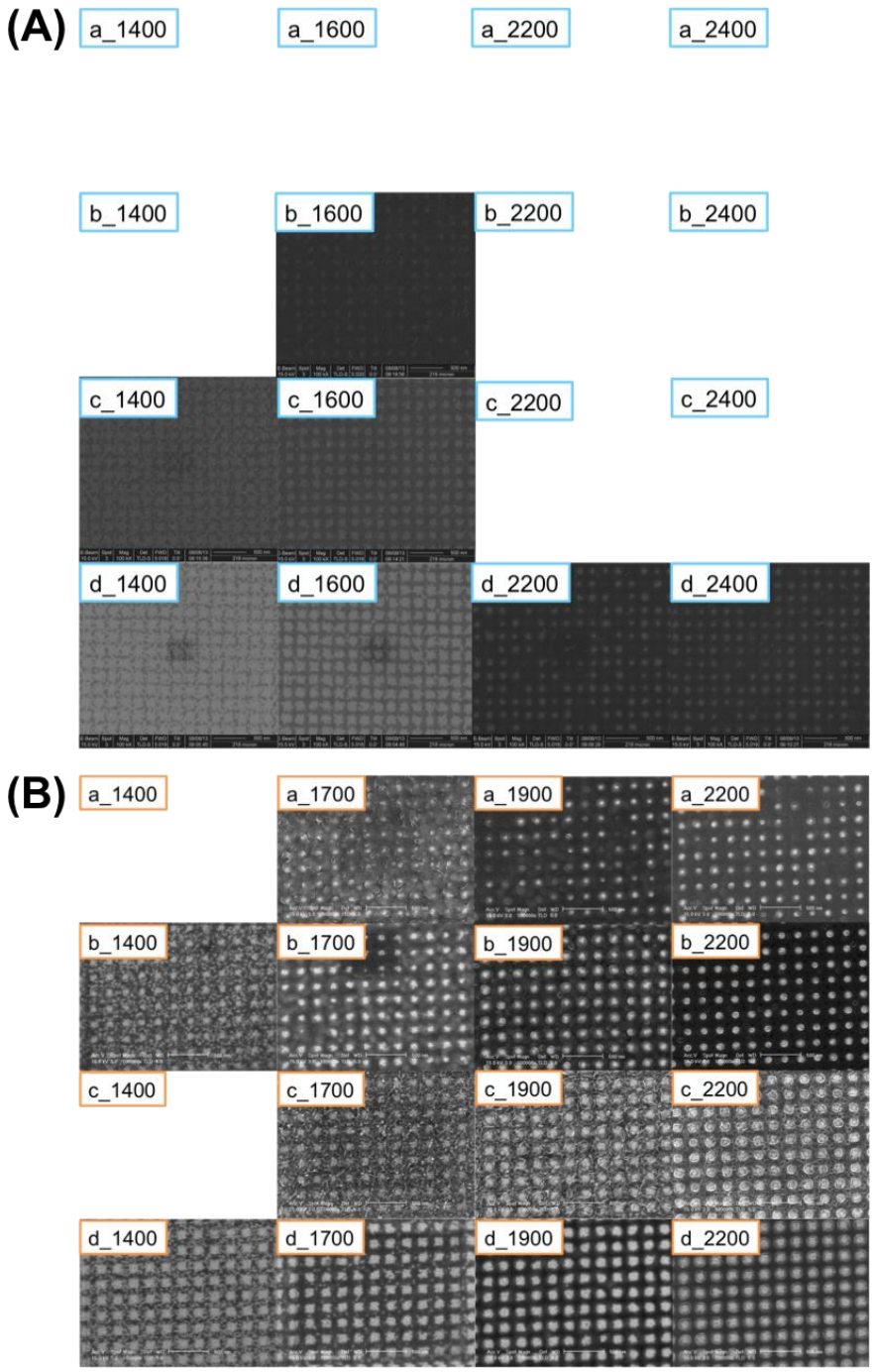
(A)
a_1400
a_1600
a_2200
a_2400
b_1400
b_1600
b_2200
b_2400
c_1400
c_1600
c_2200
c_2400
d_1400
d_1600
d_2200
d_2400
(B)
a_1400
a_1700
a_1900
a_2200
b_1400
b_1700
b_1900
b_2200
c_1400
c_1700
c_1900
c_2200
d_1400
d_1700
d_1900
d_2200

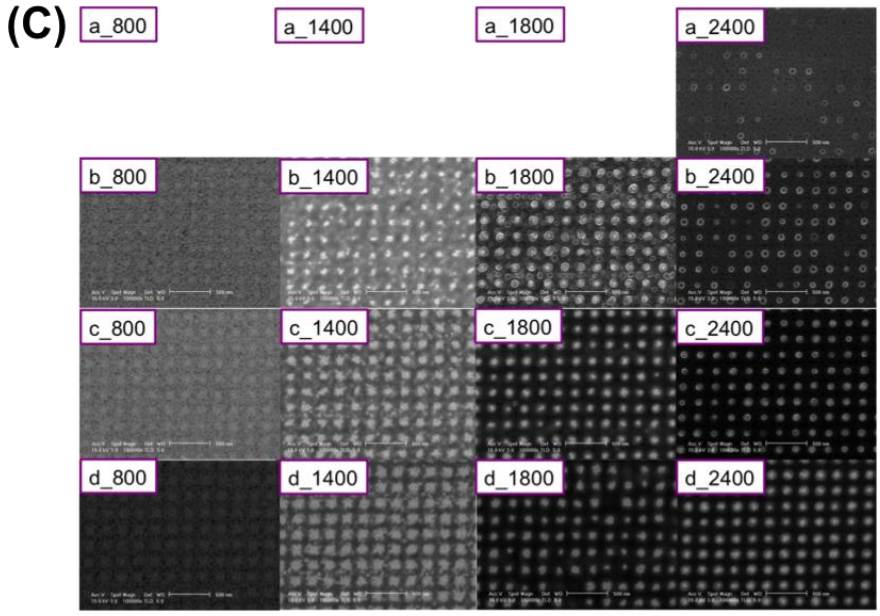

Figure 2.5 Enlargement of Figure 2.4. The patterned from 800 to 2400 (200 interval) for (A) and (C) and from 1400 to 2200 (100 interval) for (B). The absent images are due to lack of observable patterns.

2.4.2 Parameter 2: Molecular Weights of PS

Various molecular weights (MWs) of PSs were investigated. In theory, lower MWs yield better contrast but require a higher dose. The hydrodynamic volume occupied by a single polymer molecule is directly proportional to its molecular weight if we assume a monodispersed polymer solution. For a negative resist like PS, the e-beam exposure will induce polymer crosslinking, making the polymer insoluble during the developing process. There should be one crosslink per molecule on average to make the polymer completely insoluble or gelatinize. It requires fewer crosslinks to achieve gelation for polymers with higher molecular weights. Therefore, a lower electron dose is needed for the higher molecular weight polymers, which exhibit higher electron sensitivity [30].

According to Charlesby's theory [31], the threshold dose where the contrast curve starts to rise (D_0) is called the 'gel point' and is roughly inversely proportional to the molecular weight for simple negative polymer resists [29, 32, 33, 34]. This is the minimum dose required for PS to crosslink and sticks to the substrate instead of dissolving in the developer. Figure 2.3 (10,500 g/mol of PS) and Figure 2.8 (2,000 g/mol of PS) show that a smaller MW of PS requires a lot higher dose to make it stay on the substrate so that the pattern will be fabricated. The critical dose for 10,500 g/mol of PS is approximately 2,500 $\mu C/cm^2$ whereas the critical dose is approximately 10,000 $\mu C/cm^2$ for 2,000 g/mol of PS.

Three molecular weight of PS (2,500, 7,800, and 13,000 g/mol) was studied and reported in Nanotechnology in 2013 [35]. It was found that the molecular weight was inversely proportional to the contrast and sensitivity; so lower molecular weight of PS (2000 g/mol) [36] is selected to achieve higher resolution patterns.

2.5 Ar^+ Milling Test/Condition

2.5.1 Milling Test Across with 3-inch SiO_2 Wafer

Ar ion (Ar^+) milling system has a broad beam of neutral argon atoms that bombard the surface of a sample to remove material abrasively. This customized Ar^+ milling system has an ionized Ar (Ar^+) source initially so it is called Ar^+ milling system; however, Ar^+ atoms are neutralized by electrons before reacting with surface. The Ar^+ milling instrument uses a Veeco RF ion source. The process was carried out at a base pressure of 4 x 10^{-6} Torr and a gas pressure of 0.4 mTorr, with a beam energy of 500 eV and a discharge power of 50 W. The Ar^+ milling system was tested for the milling rate

and uniformity over the 3-inch wafer. The SiO_2 wafer was inserted into the system as depicted in Figure 2.6 (A). The Ar gas valve was opened, and the condition for the milling was ~32 mA for 8 min, or 15,120 Coulomb. The milled wafer shown in Figure 2.6 (B) was analyzed by ellipsometry (J.A. Woolam M-2000 spectrosopic ellopsometer). The thickness mapping of the wafer is shown in Figure 2.7. This test demonstrates that the milling is not uniform, so it is important to load the sample appropriately for consistent results.

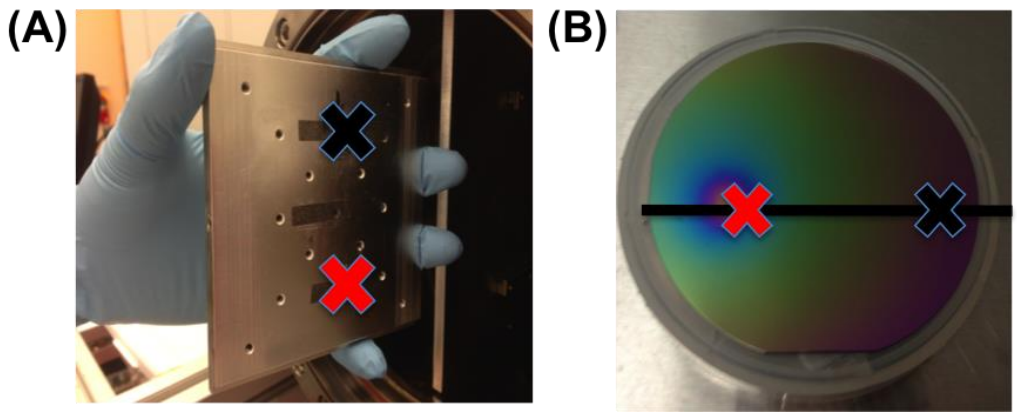

Figure 2.6 The Ar milling loading chamber with sample holder (A) and SiO_2 wafer (B) after Ar milling (500 sec with beam current 30 mA). The two x marks (red and black) indicate the position where the wafer inserted.

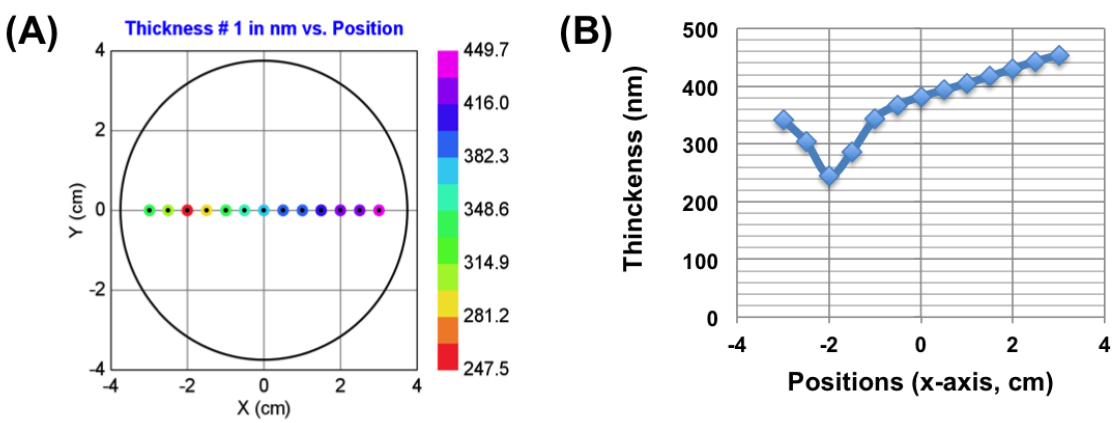

Figure 2.7 The thickness mapping of wafer shown in Figure 2.4 (B).

2.5.2 Milling Test with 2,000 g/mol PS

A Si wafer was coated with 218 nm of PS by spinning a 6 % w/w of 2,000 g/mol PS dissolved in toluene at 2500 rpm with an acceleration of 3000 rpm/s. The thickness before and after Ar milling process was measured by ellipsometry and is plotted in Figure 2.8. The etch rate can be calculated for each condition, and this is used to etch a desired amount of material.

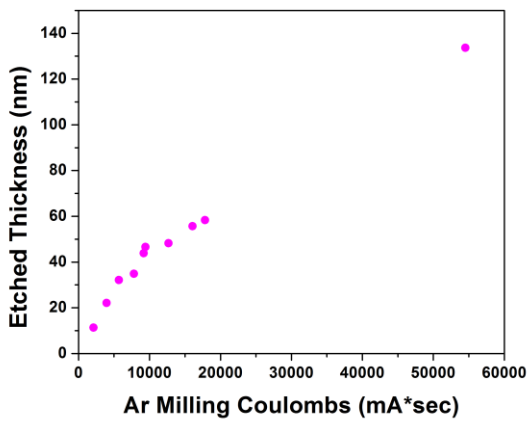

Figure 2.8 Ar milling rate test with 2,000 g/mol PS.

2.6 Experimental Results

The contrast curve for 2,000 g/mol PS is shown in Figure 2.9. The critical dose is approximately 10,000 μC/cm^2. The same dose series (shown in Figure 2.4 and 2.5) with p-xylene were tested with small MW PS (data is not shown here). The contrast was better than large MW PS as illustrated in Figure 2.9 top left as expected. Figure 2.9 shows the effects of argon milling on pattern of circles exposed at 9,000 μC/cm^2. As the pattern is milled for a longer time, the circular pattern gradually transforms into square-like patterns.

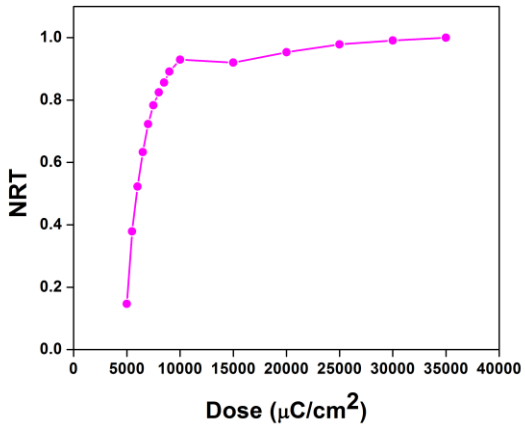

Figure 2.9 Dose series with e-beam lithography with 6 w/w % of 2,000 g/mol PS and developed by *p*-xylene.

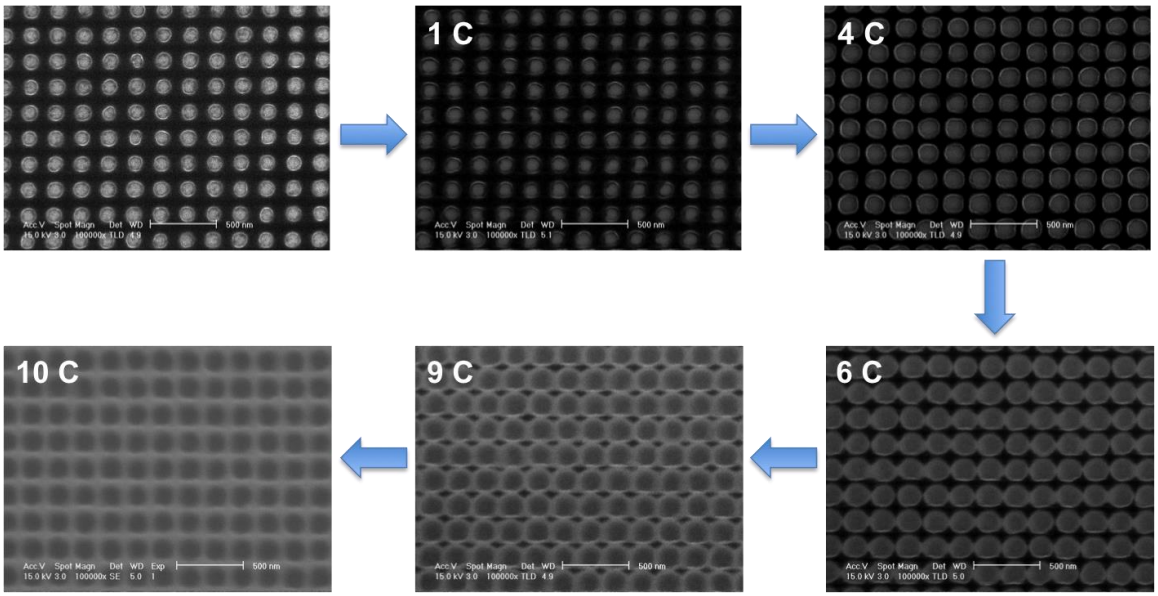

Figure 2.10 SEM images of 2,000 g/mol PS patterned with 9,000 μC/cm^2 and then Ar milling with 1 to 10 Coulomb as a total flux with ~30mA as a beam current.

2.7 Conclusions

A lithography process has been developed to fabricate non-circular patterns in PS. The production of PS patterns by e-beam lithography followed by Ar milling is a viable process for generating non-circular nanoscale patterns. However, traditional e-beam

lithography-based methods is not a viable technique toward producing the amount of bit patterns required to cover an entire disk because it is a serial patterning technique. It would simply take way too much time to print a pattern to be economically viable. The limitations are exacerbated at smaller length scales, where BPM is viable. However, a self-assembly process such as BCP can overcome the throughput limitations of e-beam lithography. Specifically, we investigate polystyrene-b-polymethyl methacrylate (PS-b-PMMA) diblock copolymer. BCPs are promising candidates for patterning nano-devices because it can spontaneously create ordered microdomains of various shapes such as spheres, cylinders, lamellae, and bicontinuous networks. However, BCP patterns are generally circular because they are thermodynamically favorable [37]. Therefore, fabricating large area of circular patterns via self assembled BCPs followed by Ar milling to fabricate the non-circular patterns is a viable strategy to fabricate large and repeated patterns that are suitable for BPM.

Chapter 3. Fabrication of Nanopatterns by Block Copolymer

3.1 Introduction

This study describes the fabrication and manipulation of polymeric materials to produce nanoscale patterns. Polystyrene-block-polymethyl methacrylate (PS-b-PMMA) block copolymer thin films were spin-coated on a silicon wafer substrate. Upon annealing, the polymer blocks self-assembled on the surface in a hexagonal array, with PMMA cylinders embedded within a PS matrix. A helium ion beam was used to degrade the PMMA polymer, enhancing the PS matrix on the surface. The PS template was strengthened by the helium ion beam due to irradiation inducing crosslinking within the film. After the removal of the degraded PMMA, we modified the templates to convert the cylindrical pores to hexagonal-shaped openings using an Ar^+ milling process. The resulting thin films was analyzed by atomic force microscopy (AFM), scanning electron microscopy (SEM), and optical ellipsometry.

3.1.1 Fundamental Theory

Block copolymers are the composites of monomers (Figure 3.1 a). The molecule grows repeatedly to become a polymer (Figure 3.1 b). If two or three different types of polymers are connected together it is called a diblock copolymer (Figure 3.1 c) or a triblock terpolymer (Figure 3.1 d), respectively.

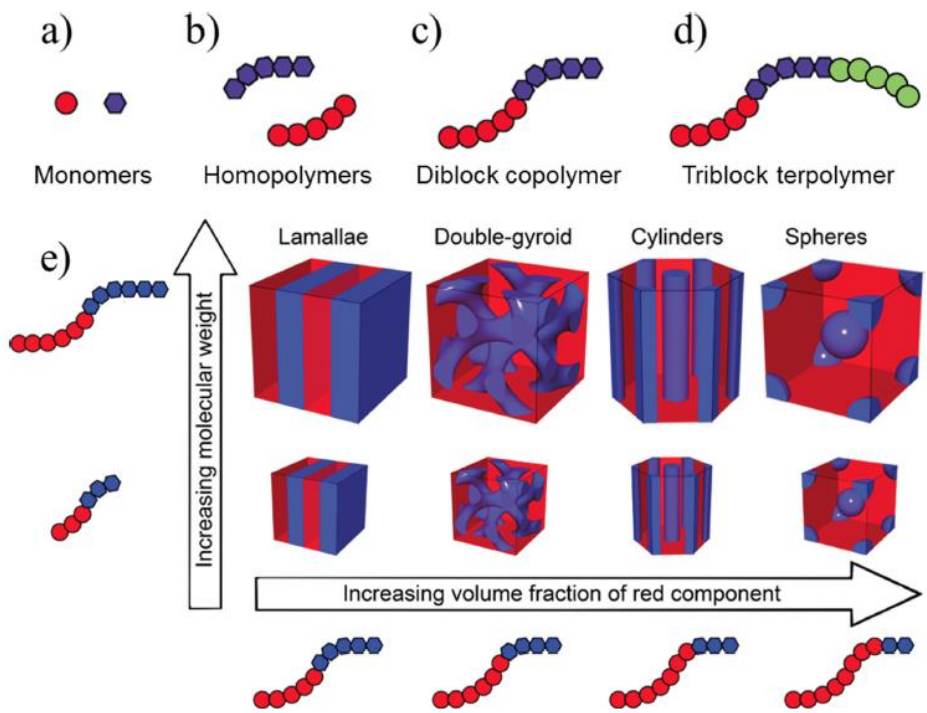

Figure 3.1 Block copolymers and self-assembled equilibrium morphologies [38].

The block copolymer is the focus of this study and equillbrium morphology and characteristic periodicity for a microphase separated diblock copolymer is shown in Figure 3.1e. The morphologies are determined by the factors of χ, N, and f where χ is Flory-Huggins interaction parameter between two blocks, N is the number of monomers in the diblock copolymer and f is the fill fraction of one or other of the two blocks (i.e., f_A or f_B). The strength of the repulsive interaction (χN) determines the propensity for block copolymers to phase separate into periodic microdomains. There is a critical point between order and disorder transitions. An order-disorder transition occurs when χN falls below a critical value when the molecular weight is small or at high temperatures (since $\chi \approx a + b/T$) [39]. In diblock copolymers, the morphology of the microdomains ranges from spheres to cylinders to lamellae depending on the volume fraction of one block. For instance, the morphologies depend on the volume fraction of red (f_A) in

Figure 3.1. The theoretical phase diagram for a linear diblock copolymer is shown in Figure 3.2 with χN versus f. The various equilibrium morphologies that minimize the thermodynamic free energy of the segregated systems are shown; lamellae (L), the double gyroid (G), hyxagonally packed cyliners (H), bodycentered cubic packed spheres (S), and closepacked spheres (CPS). The system is disordered (DIS) outside of these ordered systems [38]. The size of microdomains scales with the copolymer molecular weight [39].

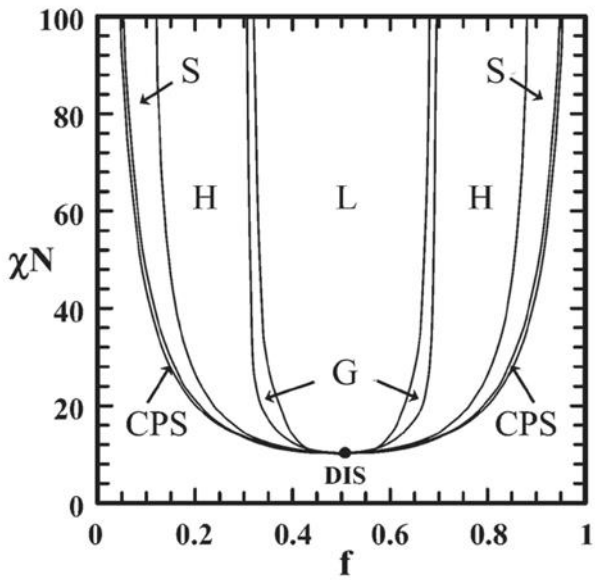

Figure 3.2 Theoretical phase diagram for a linear diblock copolymer [38].

3.2 Materials

We used the commercially available polymers from Polymer Source, Inc and used them without any further purification. The brush layers were prepared from a random copolymer poly(styrene-co-methyl methacrylate) α-hydroxyl-ω-tempo moiety terminated that is 62 wt % of PS with Mn = 7000 and Mw/Mn = 1.30. The PS-b-PMMA polymer is

poly(styrene-b-methyl methacrylate) with Mn = 64000 and 35000 for PS and PMMA respectively and Mw/Mn = 1.09.

3.3 Experimental Procedure

3.3.1 Overview of Entire Experimental Process

The most important factor for this fabrication process is to have a brush layer underneath the BCPs. The silicon substrate has a preference to PMMA since PS has slightly lower surface energy than PMMA. Thus, the straightened PMMA within a PS matrix is not a naturally favorable result. The possible outcomes from PS-b-PMMA are shown in Figure 3.3 and the perfect perpendicular orientation, Figure 3.3 (b), is desired for BPM application.

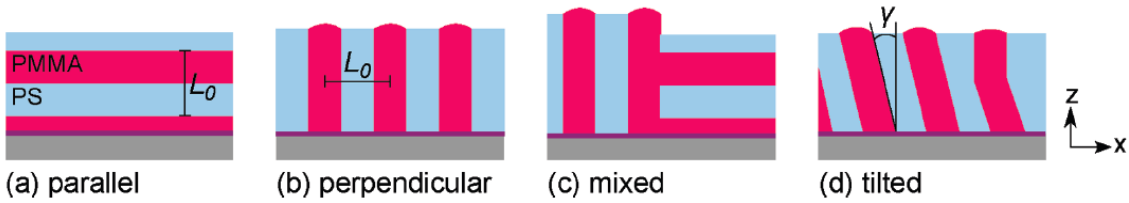

Figure 3.3 Possible outcomes from PS-b-PMMA copolymer: (a) parallel domain orientation, (b) perfect perpendicular orientation, (c) mixed paralle and perpendicular orientation, (d) perpendicular phase with tilt defects [40].

The substrate becomes "neutral" by coating the substrate with a brush layers since the substrate has no preference neither PS nor PMMA. The brush layer encourages the perpendicular orientation shown in Figure 3.3 b. The fabrication process is illustrated in Figure 3.4 below.

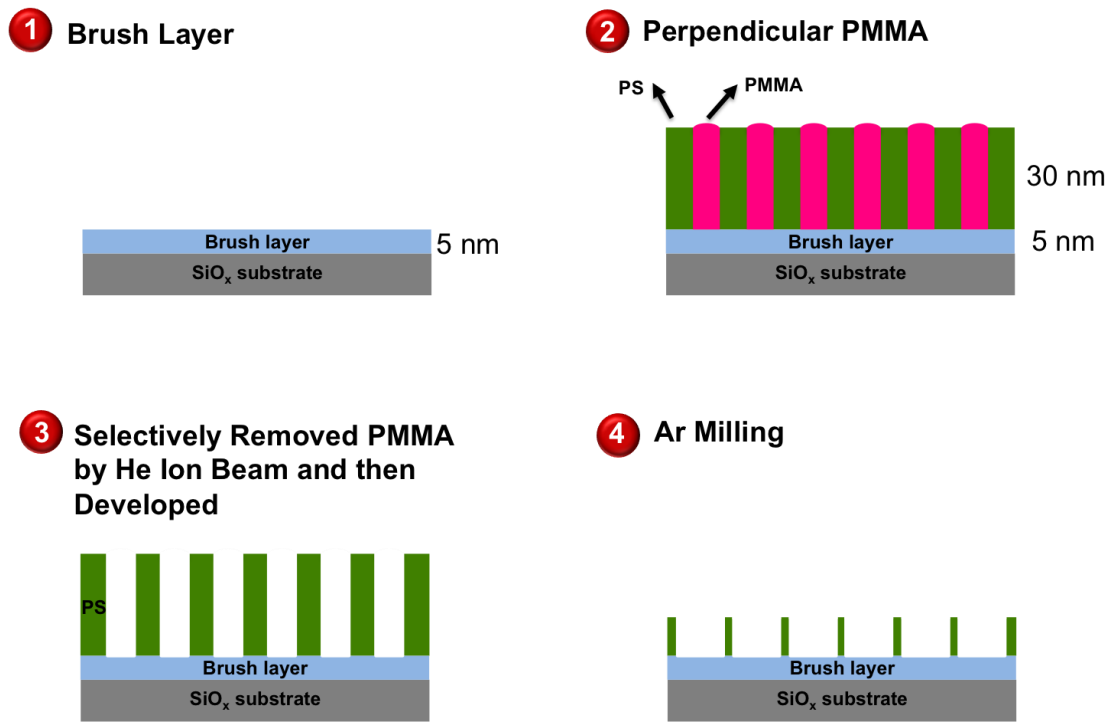

Figure 3.4 The procedure for fabricating BPM patterns using PS-b-PMMA diblock Copolymer.

Silicon wafers (Si wafer with native oxide layer) treated by UV/ozone were used as substrates. The brush layer was prepared from a random copolymer poly(styrene-co-methyl methacrylate) α-hydroxyl-ω-tempo moiety terminated that is 62 wt % of PS. This random polymer was dissolved in toluene at a concentration of 1 wt % and then prepared by spin-casting on the substrate. The brush layer spin-casted wafers were thermally annealed in a vacuum oven at 80 °C for 7 h, then at 170 °C for 24 h, and then cooled to room temperature. Any extra polymers were washed off with toluene several times. The thermal annealing process was repeated twice. The PS-PMMA BCP was prepared by spin-casting on the brush layers by dissolving in toluene at a concentration of 1 wt%. The PS-PMMA polymer was poly(styrene-b-methyl methacrylate) with Mn = 64000 and 35000 for PS and PMMA, respectively, and Mw/Mn = 1.09. The PS-PMMA BCP was

baked on a hot plate for 10 min at 240 °C without any light after the spin-casting process. The thickness of the BCP was approximately 30 nm. The self-assembled PS-PMMA BCPs were exposed to an He atom beam for 60 sec to remove the PMMA selectively to produce a nanoporous pattern in PS. Then Ar^+ milling was used to expand the circular patterns to non-circular patterns.

3.3.2 Helium Atom Beam Tool

A customized He atom beam system was used to remove PMMA selectively from PS. The distance between the source and electrostatic deflector was approximately 62 cm, and the distance between the deflectors and the stage (SmarAct GmbH, Oldenburg, Germany) was approximately 93 cm. The schematic and photo of the system is shown in Figure 3.5.

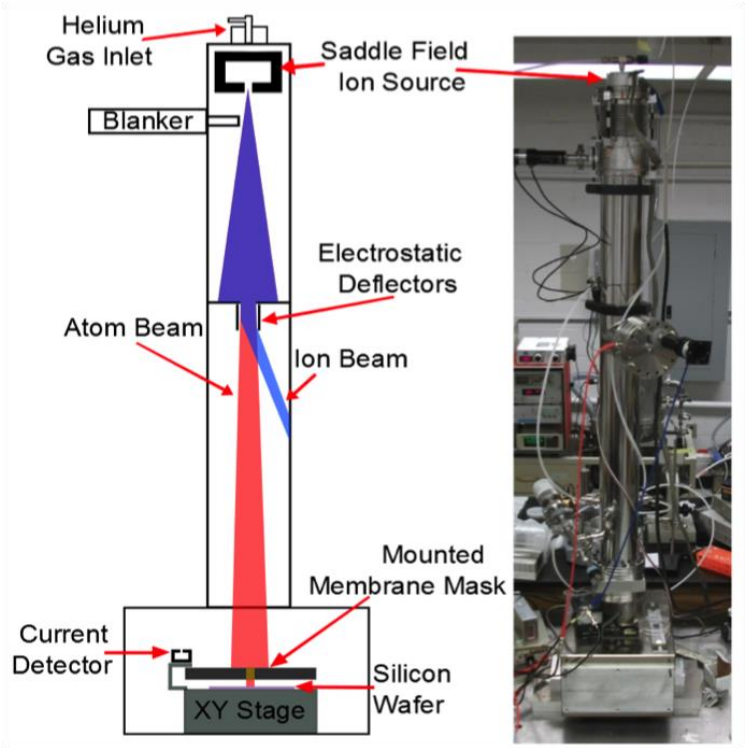

Figure 3.5 Schematic and photo of the He atom beam system [41].

The beam is uniform with 5% over a 1 inch diameter can penetrate approximately 100nm deep into the BCP. The atom beam alters the solubility of the resist. For example, this beam treatment crosslinks the PS but causes the main-chain scission of PMMA enabling acetic acid to dissolve PMMA but not PS. The source is mixture of ions and atoms and the deflectors sweep the ions out of the way. The PS-b-PMMA patterns is exposed to a beam current of 1.1 nA for 60s, followed by immersion in acetic acid for 3 min, washing with deionized water for 30 sec, and blow dried with nitrogen gas.

3.4 Results

The surface after the first step in Figure 3.4 with the brush layer was analyzed by ellipsometry and contact angle to measure thickness and ensure a successful surface modification. The contact angle is approximately 77° and the thickness is approximately 5.7 nm. In comparison, the contact angle is 37° and 9° for the Si substrate and the substrate after UV/ozone clean respectively. UV/ozone treatment of the substrate generates an increased number of hydroxyl groups on the surface of the substrate, which reacts with the brush polymer via dehydration.

The fabricated BCPs, after the second step in Figure 3.4, were characterized by scanning electron microscopy (SEM) and atomic force microscopy (AFM) and shown in Figure 3.6.

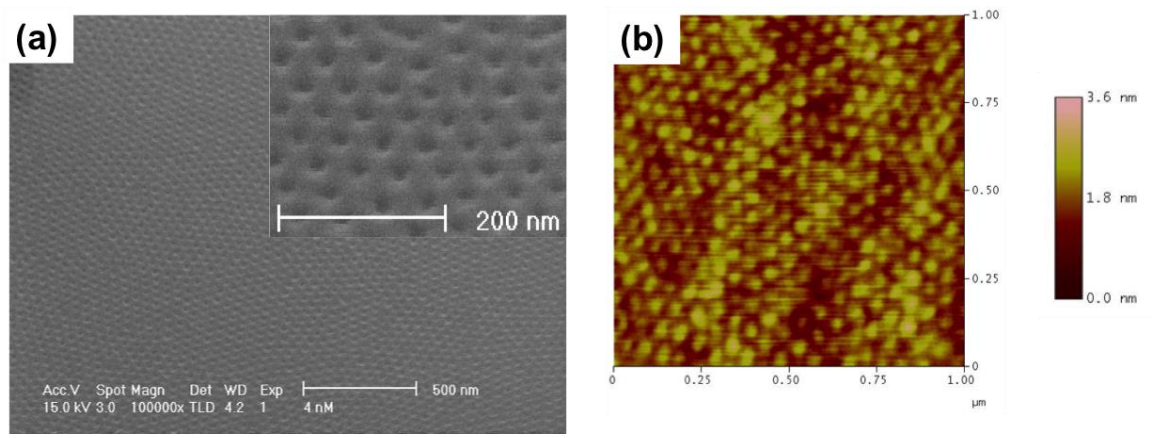

Figure 3.6 The (A) SEM and (B) height AFM images of PS-b-PMMA. These images were taken after the process (2) in the Figure 3.4.

The BCPs were treated with He atom beam for 60 and then developed by acetic acid to remove the PMMA shown in Figure 3.7. When the BCPs treated He ion beam was over exposed, 90 seconds, the patterns were destroyed as shown in Figure 3.8.

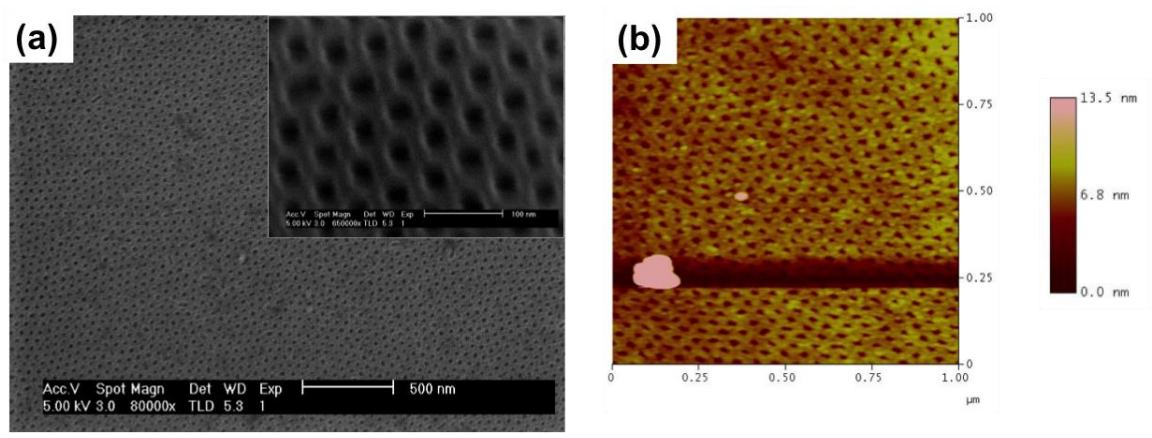

Figure 3.7 The (A) SEM and (B) height AFM images of PS-b-PMMA after He ion beam exposure for 60 sec and then washed off by acetic acid to remove PMMA. These images were taken after the process (3) in the Figure 3.4.

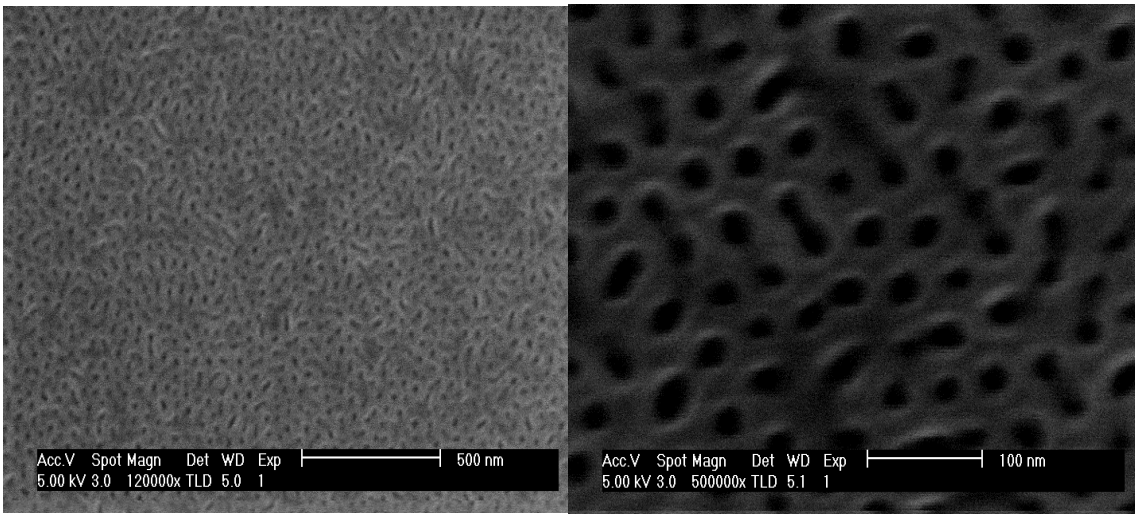

Figure 3.8 The SEM images of PS-b-PMMA after He ion beam exposure for 90 sec and then washed off by acetic acid to remove PMMA.

We fabricated a 30 nm thick PS templates with circular nanoporous (diameter of approximately 30nm) on top of a 5 nm thick brush layer. Ar^+ milling was applied to transforms the pores from circular to hexagonal. The Ar^+ milling process was optimized to determine the correct conditions to generate hexagonal openings without distorting the patterns. Figure 3.9 shows the etch rate of the BCP film when it was milled at 30 mA for various amounts of time.

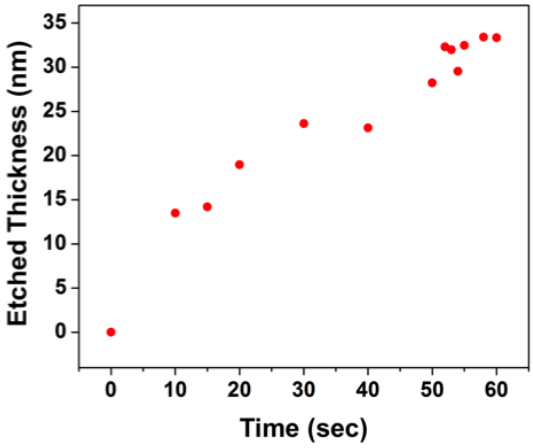

Figure 3.9 Ar^+ Milling test with 30 mA beam current of PS-b-PMMA BCP after He atom beam exposure for 60 sec with 1.1 nA.

The etch experiment revealed that the 30 nm thick BCP pattern will be completely etched within 60 seconds. The patterns were milled for 10, 20, 30, 40, 50, and 60 sec with beam current 25 to 30 mA, beam voltage 500 V, accelerator voltage 500 V and forward powder 80 W, and the AFM height and phase images of each trial is shown in Figure 3.10.

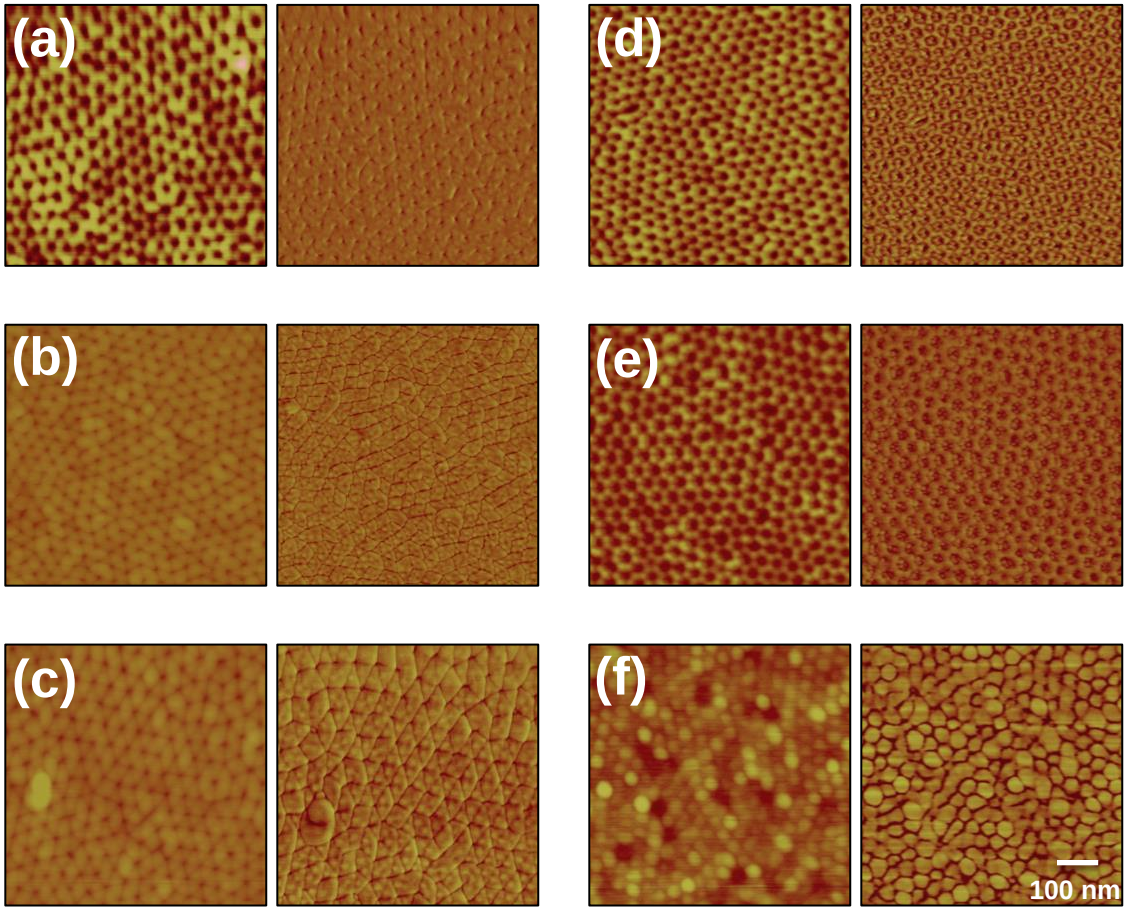

Figure 3.10 The height (left) and phase (right) AFM images after Ar^+ milling bombardment for (a) 10, (b) 20, (c) 30, (d) 40, (e) 50, (f) 60 seconds.

From the AFM images, the hexagons are visible when the milling time is between 50 and 60 seconds. However, when the pattern was milled for over 50 seconds, there was no BCP film remaining. Therefore, we need to discover a condition that can produce

hexagonal shapes in PS without etching away all the PS. Some problems we observed is that the beam current is not stable and varies 25 and 30 mA. By monitoring the beam current and integrating it over the mill time, we can achieve finer control over the milling process. This enables us to achieve the results shown in Figure 3.11.

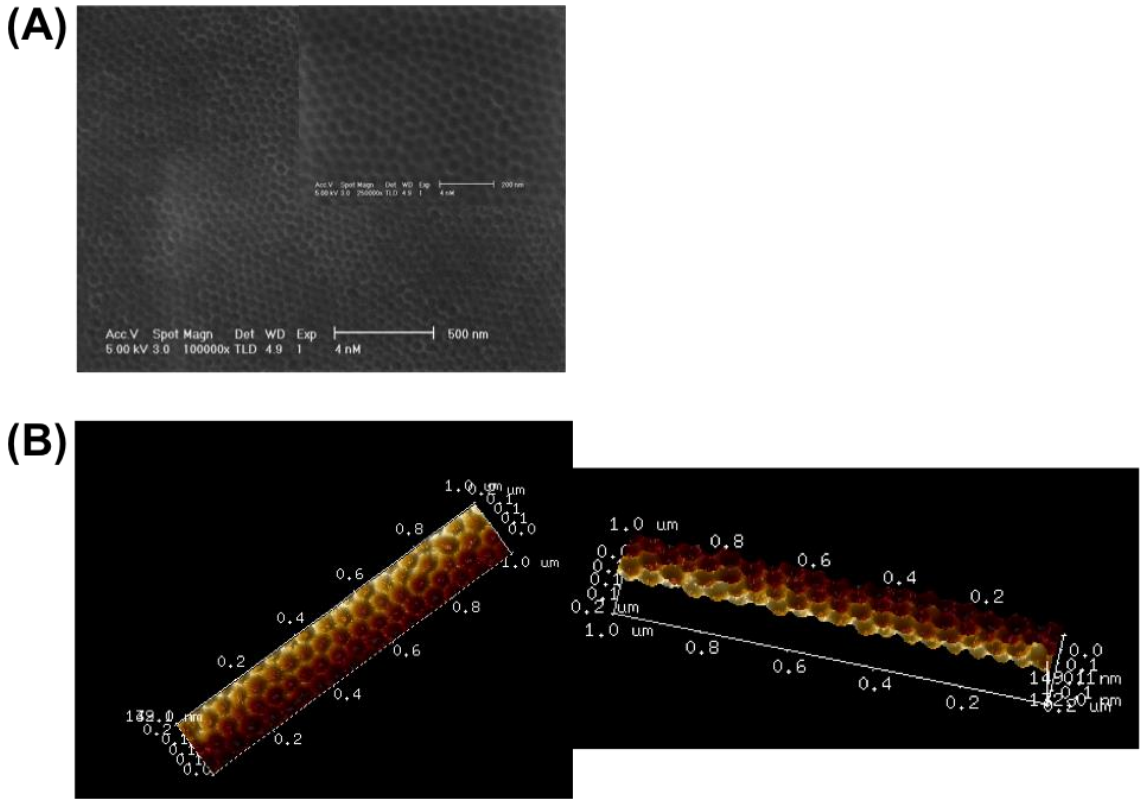

Figure 3.11 The SEM images of PS-b-PMMA after He ion beam exposure for 60 sec and then washed off by acetic acid to remove PMMA. These images were taken after the process (4) in the Figure 3.4.

3.5 Conclusions

The PS patterns fabricated by e-beam lithography with approximately 100 nm openings were studied in Chapter 2. The Ar^+ milling process was applied to transfer the circular openings to the non-circular ones. Self-assembled block copolymer process was

developed to fabricate arrays of nano-scale patterns at a much faster rate than what could be achieved via e-beam lithography. A PS film with 30 nm diameter pores was prepared, and it was successfully transformed into 40 nm hexagonal openings. These nanoscale patterns can be used for a variety of applications that require dense patterns. These nanoscale hexagonal patterns can be used as masks for patenting on other substrates or as molds so other materials such as CoPd or FePt can be filled inside.

Chapter 4. Spin-Glass Behavior in Graphene Oxide Powders Induced by Non-Magnetic Sodium Sulfate

4.1 Introduction

Graphene is composed of a conjugated carbon atom network with a honeycomb crystal lattice, bond lengths of 1.42 Å, and a thickness of only one atom [42]. Certain properties of graphene, such as low spin-orbital coupling and zero nuclear spin of the naturally abundant ^{12}C isotope, are favorable for spintronic applications. These properties give rise to a large spin diffusion length and long coherence times, [18-20] which are crucial for quantum information manipulation and quantum computing [18, 22].

Prior research has shown that graphene possesses unique electrical [43], mechanical [44], thermal [45], and optical properties [46], but there are few studies regarding the magnetic properties of graphene. Consequently, there is a need to advance the understanding of the magnetic properties of graphene and its derivatives and to develop the ability to tune such properties, enabling prospective applications of graphene-based materials in nanomagnetoelectronic, spintronic [17, 24, 25] (such as spin memory, transistors, and perhaps solid–state qubits) [18, 19, 25, 47], magnetoresistance, and magnetic memory devices [47, 48].

Recent research has shows that defect-free graphene with so-called "zig-zag edges" exhibits no detectable magnetic behavior. Apparently, irregularities in the carbon

bonding network, such as covalently bonded moieties that disrupt the network [49], along with other defects and structural discontinuities in the aromatic network, are essential for magnetism to be present in graphene [50]. These irregularities are known to play an important role because they can induce spin polarization in systems that typically possesses high levels of symmetry [51]. Therefore, developing controlled methods of disrupting the graphene carbon bonding network is essential to induce and tune the magnetic properties. It is also important that the targeted magnetic states be stable at room temperature for most magnetic applications [52].

A more detailed analysis of the root causes for the magnetism exhibited by certain forms of graphene can be conducted by categorizing these causes into three types: defects associated with the graphene atomic structure (topological defects) [51-53], defects caused by atoms/molecules attached to graphene or substitutuent C atoms [54-56], and irregularities at the edges [54] of the graphene sheet. Unfortunately, studies providing experimental magnetic data are rare.

Chemical functionalization [57] is one of the most experimentally accessible ways to introduce systematic defects into pristine graphene. This method is not only useful to introduce defects, but it is also efficient for dispersing graphene in organic solvents or water. In addition, it can be used to produce nanocomposites and to decorate graphene with various molecules suitable for various applications. For example, diazonium salts have been widely used for the chemical functionalization of graphene [58]; Haddon et al. demonstrated that diazonium functionalization of graphene on a "substrate" can be used to tune the magnetic properties [59, 60]. Separately, other researchers have focused on "free-standing" graphene sheets, rather than graphene on a substrate [61]; however, there

was no analysis of the magnetic properties in these reports. Besides diazonium salts, Chua et al. recently explored the modification of graphene with thiols [62], but again performed no magnetic characterization of these samples. While these methods are well understood and accepted, the production of quantities of functionalized graphene sufficient for magnetic characterization and in eventual technological applications remains an ongoing challenge.

In this study, we demonstrate experimentally that non-magnetic SS induces magnetism in GO by means of a simple chemical functionalization process. Oxidized graphene (or GO) flakes prepared in an aqueous phase using Hummer's method dispersed in an aqueous phase (please see the Supporting Information for details) were used in this study. Several different oxygen functional groups are present on both sides of the GO basal planes and edges, providing ample sites for chemical reaction and functionalization [63]. Non-toxic "green", readily available, inexpensive, and stable, SS was used to modify GO, allowing a systematic investigation of the impact of this chemical species on the magnetic properties of GO.

4.2 Materials and Methods

4.2.1 Materials

We used an aqueous solution of GO that was commercially available from Graphene Supermarket: a 175 mL solution of highly concentrated single-layer graphene oxide was prepared using Hummer's method. Sodium sulfate was purchased from Sigma-Aldrich (ACS reagent grade, ≥ 99.0%, anhydrous, granular, CAS: 7757-82-6).

Acetone and acetonitrile were purchased from Sigma-Aldrich, and ethanol was acquired from Decon Labs, Inc.; all three solvents were used as received. Water was purified to a resistivity of 18 MΩ·cm by use of an Academic Milli-Q Water System (Milli-Q water; Millipore Corporation) and filtered through a 0.22 μm membrane filter before use. Flat gold substrates used for XPS analysis were prepared by the thermal evaporation of gold (~1000 Å) onto chromium-coated (~100 Å) Si wafers under ultrahigh vacuum. The gold-coated wafers were cut into slides (1 × 1 cm), rinsed with ethanol, and dried with ultrapure nitrogen gas before depositing the GO samples on top.

4.2.2 Preparation of Graphene Oxide Flakes

The commercially obtained GO in aqueous phase was diluted to 0.24 wt% by adding Milli-Q water and then sonicating for 1 h. During sonication, the temperature was kept below room temperature (rt) by constantly adding ice to the sonicator reservoir to diminish the possibility of side reactions that might occur from heat generated by the sonication process. The sonicated GO samples were then degassed for 3 h using Ar while stirring the GO solution. The 0.24 wt% GO starting solution contained ~1.5% sulfur (with ~0.004 S/C ratio as determined by XPS) arising from the Hummer's' process, which uses sulfuric acid to prepare the GO.

4.2.3 Reaction Conditions and Sample Abbreviations

A 15 mL portion of a degassed and homogeneously dispersed 0.24 wt% GO aqueous solution was mixed with 0.15 g of SS. This mixture was protected from the atmosphere to avoid further oxidation by purging the solution with Ar for 30 min. Separate 15 mL samples of this mixture were prepared and then either maintained at

23 °C or heated to 40 or 80 °C for 48 h in a closed system while stirring. The resulting solutions appeared light brown (23 °C), brown (40 °C), or black (80 °C), depending on the reaction conditions. After cooling to rt, these solutions were opened to the atmosphere for the washing steps. The GO products in aqueous solution were then centrifuged for 1 h at 10,000 rpm, with the resulting supernatant being discarded, and the GO products redispersed in acetone. The washing steps were repeated using acetone, acetonitrile, ethanol, and Milli-Q water to remove any excess SS in solution or any physisorbed SS. Samples of GO processed without adding SS were also prepared as described above and washed using the same procedure to ensure that these control samples were exposed to the same conditions as the samples that contained SS. The washed GO samples were finally redispersed in Milli-Q water followed by drying in a vacuum freeze dryer. The final products were either a brown or black fluffy powder, depending on the degree of deoxygenation of the GO (i.e., a more deoxygenated GO sample appeared as a blackish powder). All characterization was conducted on these final powders. The sample abbreviations used in this report are shown in Table 4.1. The number following the GO notation corresponds to the temperature in °C at which the samples were treated both with and without SS.

Table 4.1 Abbreviations for the GO Samples and Their Reaction Conditions

sample abbreviation	treated with SS	reaction temperature (ºC)
GO-23	no	23
GO-40	no	40
GO-80	no	80
SS-GO-23	yes	23
SS-GO-40	yes	40
SS-GO-80	yes	80

4.3 Results and Discussion

4.3.1 Characterization of Magnetic Properties

4.3.1.1 Instrument and Conditions: Physical Property Measurement System

A Quantum Design Ever Cool–II PPMS was used to collect the vibrating sample magnetometry (VSM) data to obtain the hysteresis loops. The VSM data were collected for 10 mg samples at 300 K and 5 K while the external magnetic field was swept over the range of ± 90,000 Oe at a rate of 100 Oe/sec. The PPMS was also used to generate the zero-field-cooled (ZFC) and field-cooled (FC) curves. The ZFC and FC curves were obtained over the temperature range from 3 K to 300 K, while keeping the external magnetic field at either 100 Oe or 1T. During the first step, the temperature was lowered from 300K to 3K at a rate of 5 K/min without applying any external magnetic field. After the temperature stabilized at 3 K, an external magnetic field of either 100 Oe or 1T

was applied. The ZFC curve was recorded as the temperature was increased at a rate of 3 K/min while applying an external magnetic field. After the temperature reached 300 K, the collection of data shifted to the FC curve while still applying the external magnetic field as the temperature was decreased to 3 K at a rate of 3 K/min.

4.3.1.2 Magnetic Properties

We obtained the magnetization (M-H) loops applied magnetic fields of -9 T to +9 T at room temperature shown in Figure 4.1A for the samples listed in Table 4.1. The linear part of the signal was subtracted as described elsewhere [56, 60, 64] and shown in Figure 4.1B to illustrate the saturation magnetization.

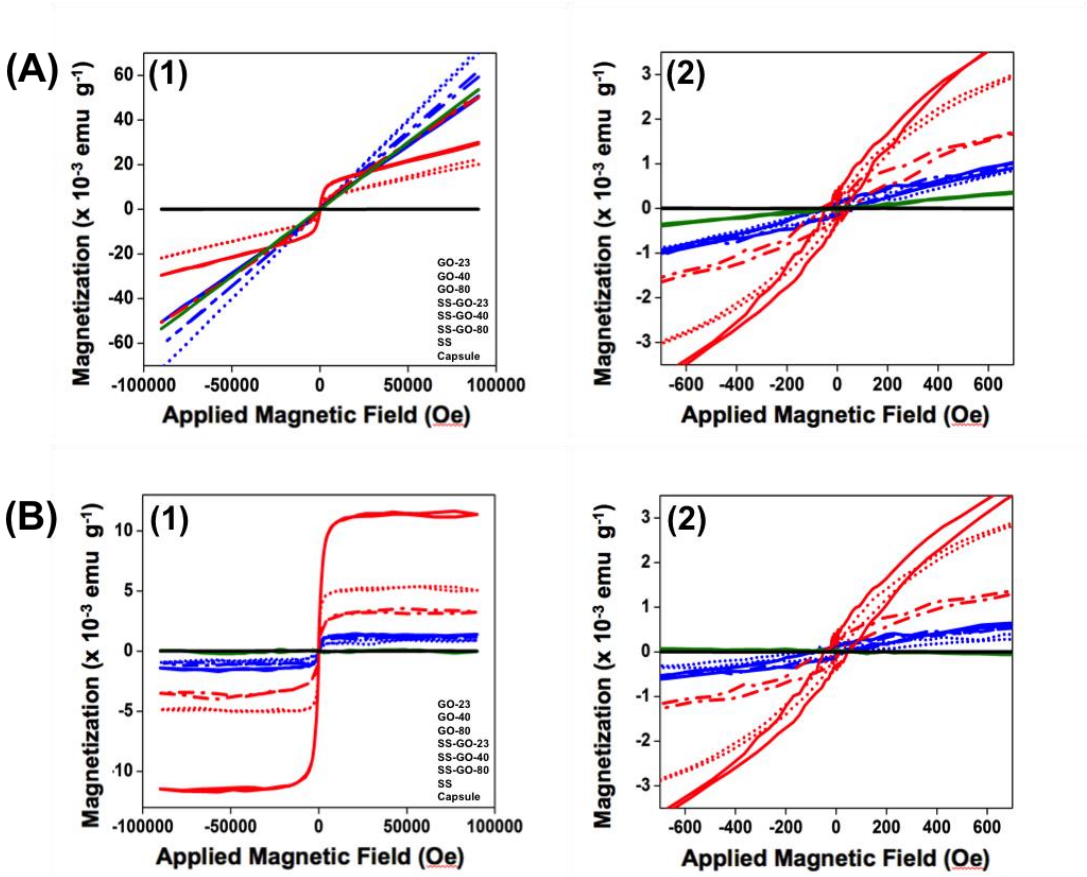

Figure 4.1 Hysteresis loops (A) after subtracting the capsule including background, and (B) after subtracting linear signal. Enlarged plots providing data for ±700 Oe from each (1) are plotted in each (2).

As can be determined from the loops, unmodified GO samples show little or no hysteretic behavior, which is typical for paramagnets. The pure SS compound measured alone has a negligible magnetic moment. The saturation magnetization values (M_S) and susceptibility (χ) for all of the samples were obtained from Figure 4.1B, and the resulting data were plotted in Figure 4.2. Samples modified with SS showed higher M_S and χ (at H = 0) values compared to non-SS-modified GO samples at room temperature. Compared to **GO-23**, the M_S values increased 3, 6 and 2 times, and the χ values increased 13, 12, and 6 times for **SS-GO-23**, **SS-GO-40**, and **SS-GO-80**, respectively, upon modification with SS.

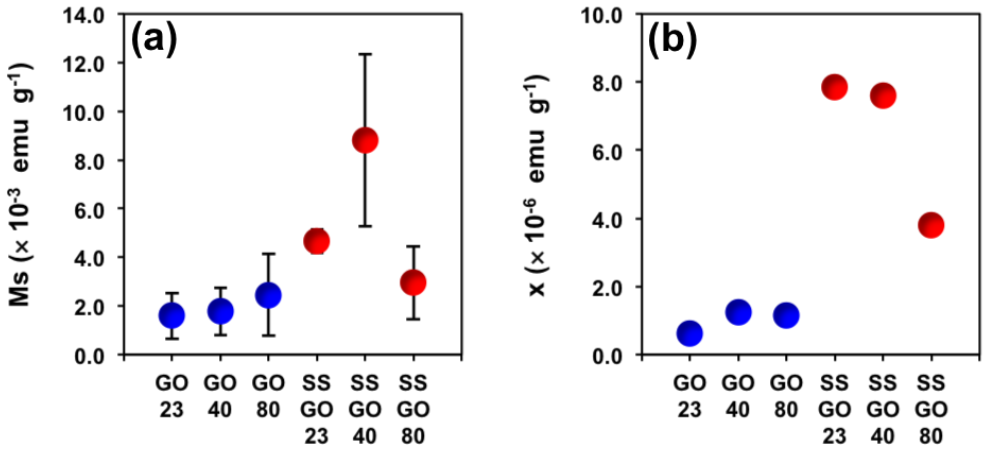

Figure 4.2 Magnetic data from Figure 1B: (a) saturation magnetizationand (b) magnetic susceptibility at zero applied external magnetic field. Error bars are not visible when the error falls within the symbols.

To gain better insight into the magnetic properties of both GO and SS-modified-GO, we performed a set of additional magnetic measurements that allowed us to collect zero-field-cooled (ZFC) and field-cooled (FC) curves (magnetization as a function of temperature), which are shown in Figure 4.3. The ZFC-FC curves provide a method for

measuring the magnetization while the temperature is rising or decreasing in the presence of an external magnetic field. The analysis of these data does not require the subtraction of the linear signal, which renders these results relatively free from artifacts [65].

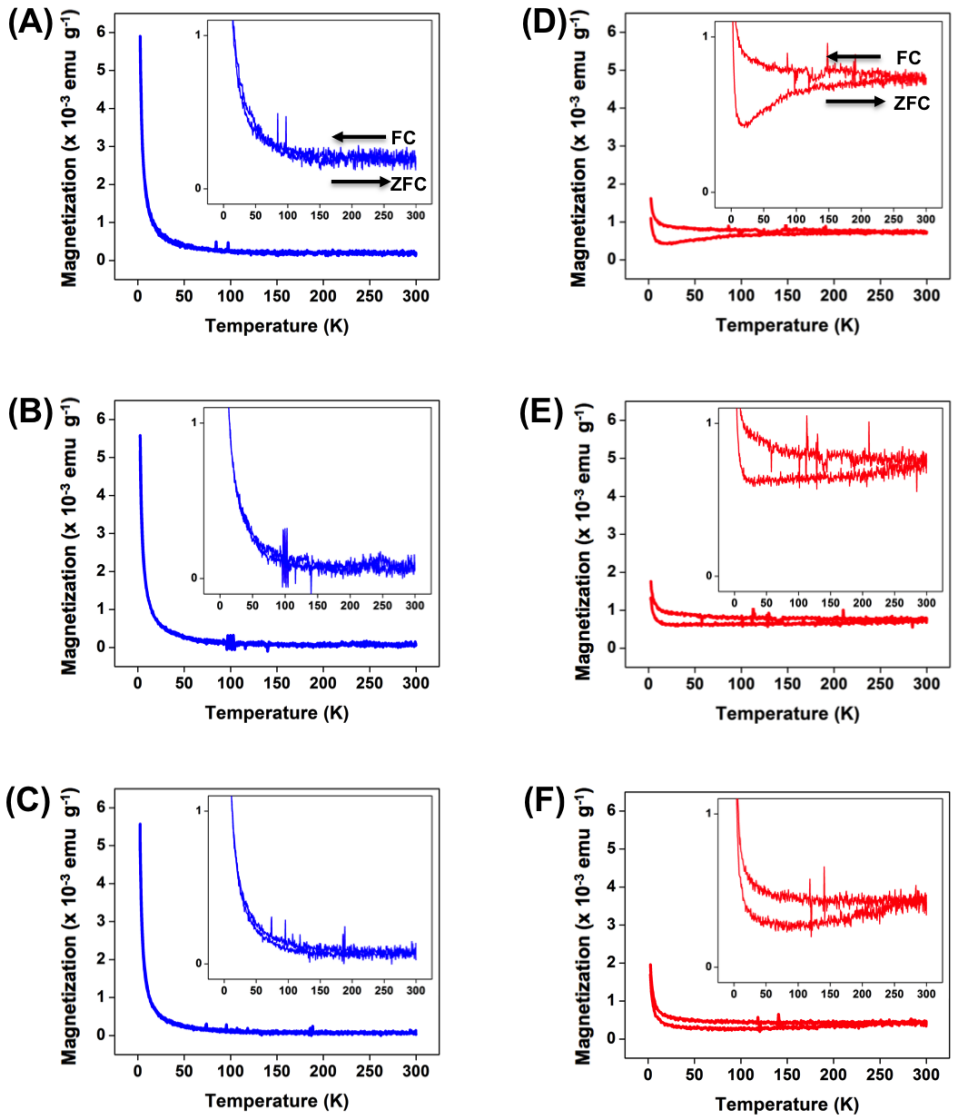

Figure 4.3 The ZFC/FC data with applying a magnetic field of 100 Oe: (A) **GO-23**, (B) **GO-40**, (C) **GO-80**, (D) **SS-GO-23**, (E) **SS-GO-40**, and (F) **SS-GO-80**. The inserts for each plot provide an enlarged from a magnetization of 0 to 1.

An analysis of the dependence of the magnetic moment of functionalized and unmodified GO samples on temperature allows identification of the magnetic phases present in the samples. The behavior of the unmodified GO samples is consistent with a paramagnetic material [66] and can be fitted with Curie's law, which is described by Equation 4.1:

$$M = \frac{C}{T-\theta} + \chi_0 \,, \tag{4.1}$$

where M is the magnetic moment, T is absolute temperature, θ is Curie-Weiss temperature, C is a material dependent constant, and χ_0 is a temperature-independent term. The linear dependence of magnetization on inverse temperature confirms our assumption of paramagnetism in the pristine GO samples, **GO-23**, **GO-40**, and **GO-80** (see Figure 4.4).

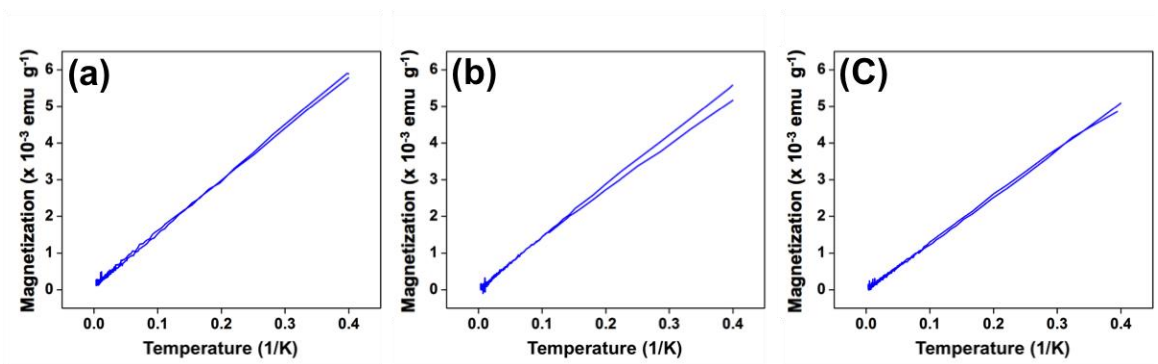

Figure 4.4 Linear dependence of magnetization on inverse temperature for (a) **GO-23**, (b) **GO-40**, and (c) **GO-80.**

There are several salient differences between the untreated samples (plots A, B, and C in Figure 4.3) versus the SS-treated GO samples (plots D, E, and F in Figure 4.3). Non-zero magnetization of the SS-treated samples can still be observed at room

temperature as compared to the untreated samples, which show negligible magnetization at room temperature. Another difference is the separation between the ZFC and FC curves. Both the ZFC and FC data follow similar trends for the untreated samples, but there is clearly separation of the FC and ZFC curves for the SS-treated samples. The divergence between the FC and ZFC curves indicates that a disordered magnetism exists [55], which is comparable to that in magnetically frustrated systems. Therefore, the divergence that appeared only for the SS-modified GO samples suggests that the reaction with sulfate triggers some form of disordered magnetism in the sulfate-modified GO samples. Several researchers have concluded that coexisting phases are induced by disordered magnetism in modified graphene [56, 59, 60, 67]. Based on our results, we propose that modification by SS introduces spin glass-like phases in paramagnetic GO.

We collected ZFC-FC curves using applied fields of 100 Oe and 1 T for the SS-modified samples, and then subtracted the paramagnetic part of the signal from the initial ZFC-FC curves to assess the properties of the spin-glass phase in greater detail (see Figure 4.5). Comparing the ZFC-FC curves obtained for at each applied field, a larger gap between ZFC and FC and a shift of the point at which the curves split toward lower temperature values was observed in the case of 1 T. Such behavior is typical for frustrated magnetic systems, which further corroborates our proposal of the presence of spin-glass phases and/or superparamagnetic phases in our samples [68]. A bend (marked with dashed lines) in the ZFC-FC curves obtained at 1 T and lower temperatures can be observed (Figure 4.5B, marked regions). This bend likely arises from a deviation in the paramagnetic phase behavior from Curie's law at high applied field and low temperature. This assumption is supported by the absence of such a jump in magnetization in the ZFC-

FC curves obtained at 100 Oe, where the applied magnetic field is insufficient to saturate the paramagnetic phase. Cartoons illustrating the spins of the samples during the ZFC/FC experiments at both 100 Oe and 1T are shown in Figures 4.6, 4.7, and 4.8.in section 4.4.4 below.

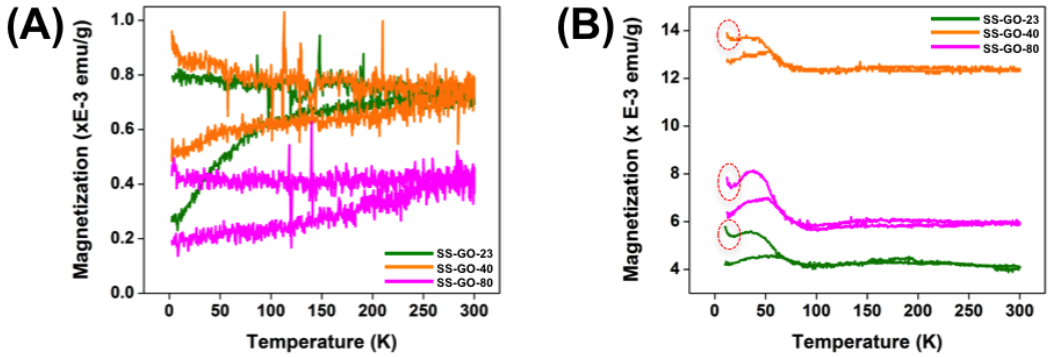

Figure 4.5 ZFC/FC curves of the sulfate-modified-GO samples (**SS-GO-23**, **SS-GO-40**, and **SS-GO-80**) with applied magnetic fields of 100 Oe (A) and 1 T (B) after subtracting the paramagnetic parts.

Assuming a simple general expression for the coercive field, H_c ~K/M, where K is the magnetic anisotropy of a material and M is the magnetic moment, Figure 5 shows that in the low temperature range (3K to ~15K), the behavior of the system is dominated by the rapidly decreasing (M~1/T) magnetic moment of the near-saturated paramagnetic phase which leads to the increase of the coercivity. In the temperature range of ~15 K to 30 K, the frustrated magnetic phase shows the strongest influence on the magnetic behavior of the system, as the moment of the paramagnetic part reaches low values leading to high values of H_c. At room temperature or above T_c (the glass transition temperature), the system again shows more paramagnetic character as the spin-glass is "softened" by thermal agitation.

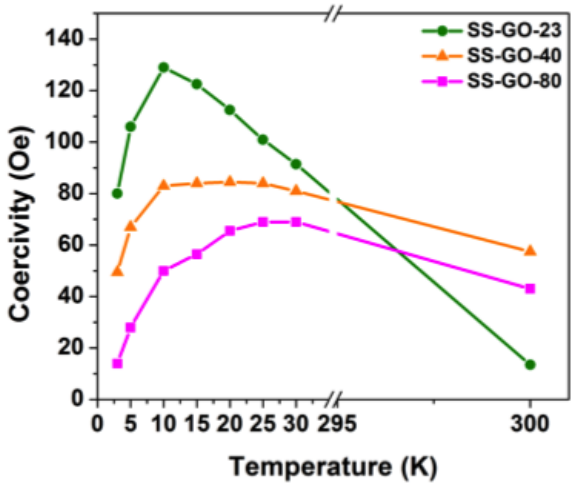

Figure 4.6 The coercivity values for the sulfate-modified-GO samples; **SS-GO-23**, **SS-GO-40**, and **SS-GO-80.**

4.3.1.3 ZFC/FC with Spin Illustrations

The samples, **GO-40** (see Figure 4.7) and **SS-GO-40** (see Figure 4.8 and 4.9), are shown in microscale with respect to spins. The arrows inside the circles stand for the spins and the arrows outside of the circle are the applied external magnetic field with direction. There is no applied magnetic field for stage 1 and 2, but 100 Oe (for Figure 4.7 and 4.8) or 1T (for Figure 4.9) is applied from stage 3 until the end of the ZFC/FC. The spins are vibrating at room temperature (stage 1) but mostly frozen at 3K (stage 2). After the external magnetic field applied, the spins reacts differently for non-modified GO (**GO-40**) and sulfate-modified-GO (**SS-GO-40**).

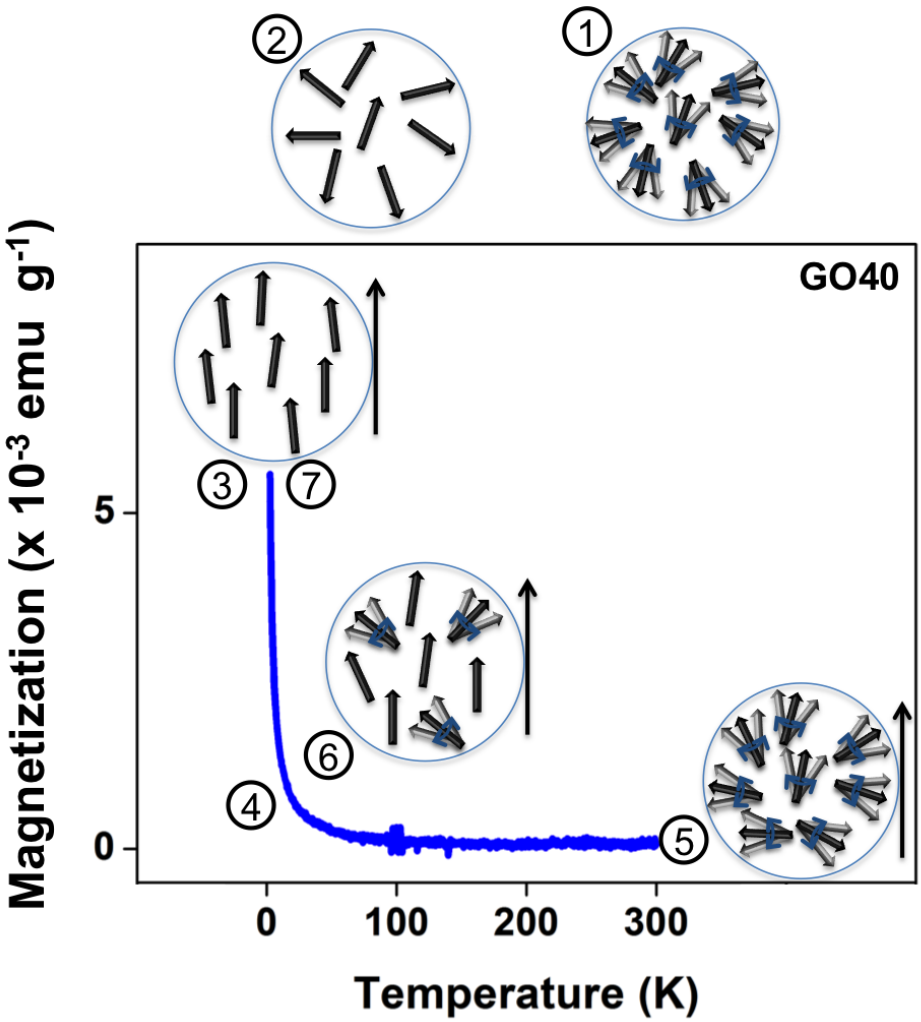

Figure 4.7 ZFC/FC obtained with 100 Oe for **GO-40**.

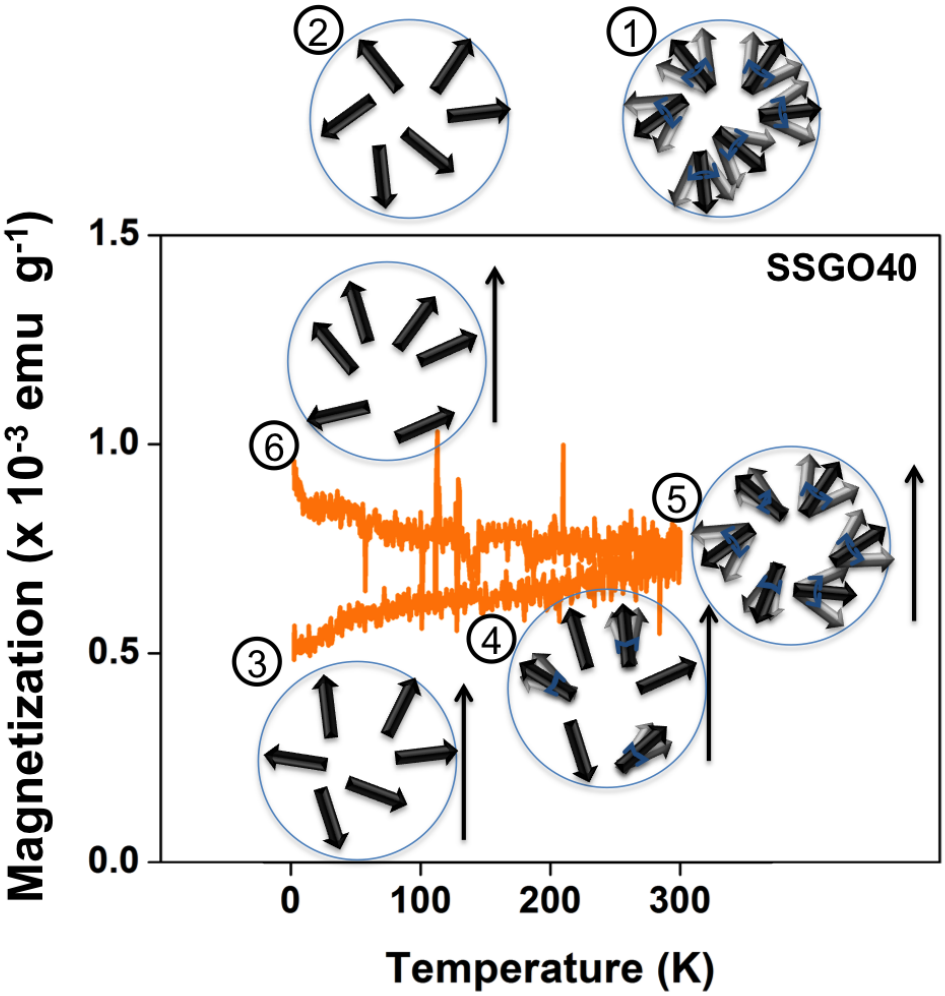

Figure 4.8 ZFC/FC obtained with 100 Oe for **SS-GO-40** after subtracting the paramagnetic behavior.

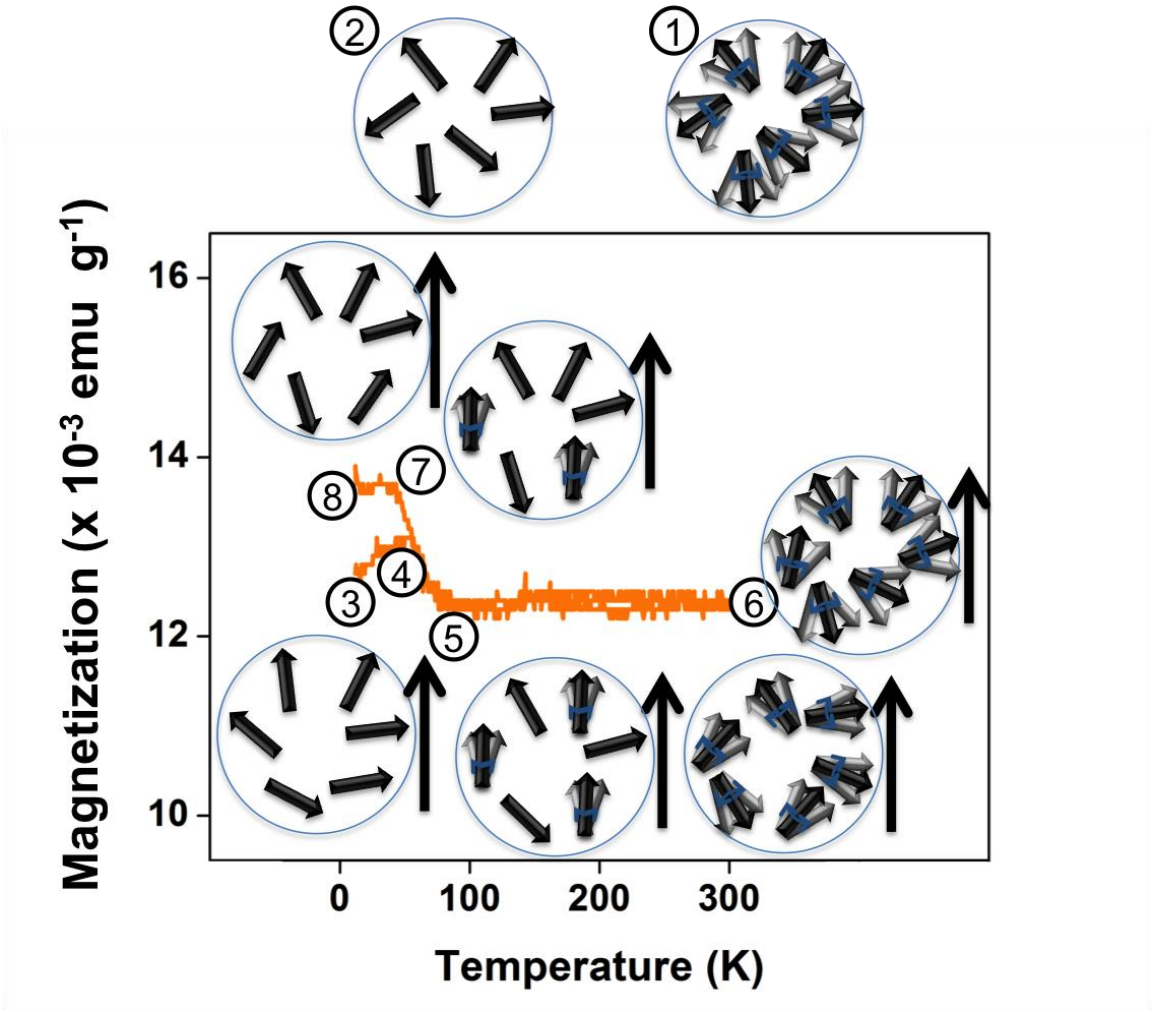

Figure 4.9 ZFC/FC obtained with 1 T of **SS-GO-40** after subtracting the paramagnetic behavior.

4.3.1.4 Conclusions from Magnetic Data Observation

The presence of the frustrated magnetic structure in SS-modified GO is likely due to the formation of localized spin-polarized electrons attracted to positively charged sites formed by the covalently bound electron-withdrawing sodium sulfate groups. A relatively low ratio of sulfur to carbon (~0.01 to 0.06 depending on the reaction temperature; vide infra) suggests the case of a dilute magnetic system with interaction between sodium sulfate-induced magnetic sites governed by Ruderman-Kittel-Kasuya-

Yosida (RKKY) interactions [69, 70]. The S/C ratios noted above are consistent with an average distance between sodium sulfate groups of about 2.5 and 6 graphene lattice constants, respectively. Dependence of the strength of the RKKY interaction on the distance between magnetic impurities and the oscillatory behavior of its sign (positive or negative) leads to the spin-glass behavior of the system. To gain a better understanding of the trends associated with the magnetic properties, we further analyzed the samples by X-ray photoelectron spectroscopy (XPS), Raman spectroscopy, and infrared (IR) spectroscopy.

4.3.2 Structural Characterization Using XPS

4.3.2.1 Instrument and Conditions: High Resolution X-Ray Photoelectron Spectroscopy (XPS)

XPS data were collected on gold substrates using a Physical Electronics Model 5700 XPS instrument with a monochromatic Al Kα X-ray source ($h\nu$ = 1486.6 eV) at 350 W and at a residual pressure of 5×10^{-9} Torr or less. The photoelectrons were collected at a 45˚ take off angle with respect to the 0.8 mm analyzed area of the sample surface and a collection cone was 5˚. All spectra were recorded at room temperature while applying a pass energy of 11.75 eV. Use of this instrument with these parameters allow an energy resolution better than 0.51 eV. The binding energies were referenced to that of the Au $4f_{7/2}$ peak at 84.0 eV. Multipak™ software was used for data processing with Shirley background subtraction applied throughout.

4.3.2.2 Characterization of Samples by XPS

XPS is one of the most effective tools for investigating the elemental composition of materials, and in this case, to determine what happened to the surface of GO when it was treated with SS at different temperatures. The C 1s, O 1s, and S 2p spectra were collected as described above, followed by an analysis of the nature and relative presence of each of the carbon, oxygen and sulfur species. Because carbon is the only element in the structure of pristine graphene, it presumably can provide good reference data for the analysis of GO by XPS. The fact that carbon is the substantial constituent of GO also justifies the use of the XPS data for carbon from which to normalize the data for oxygen and sulfur (i.e., to yield O/C and S/C peak intensity ratios), enabling comparisons between the different XPS data sets for the various graphene samples prepared. To optimize the precision of the binding energy (BE) data used in these comparisons, all of the peaks were referenced to the Au $4f_{7/2}$ peak at 84.0 eV, which is convenient because there can be a shift in the measured BEs associated with surface charging due to the electrically insulating nature of GO [71].

The C 1s, O 1s, and S 2p spectra obtained from the samples were collected (see Figures 4.10 and 4.11). Based on these spectra in Figure 4.10 and 4.11, we plotted the intensities of the C 1s peaks in Figure 4.12.

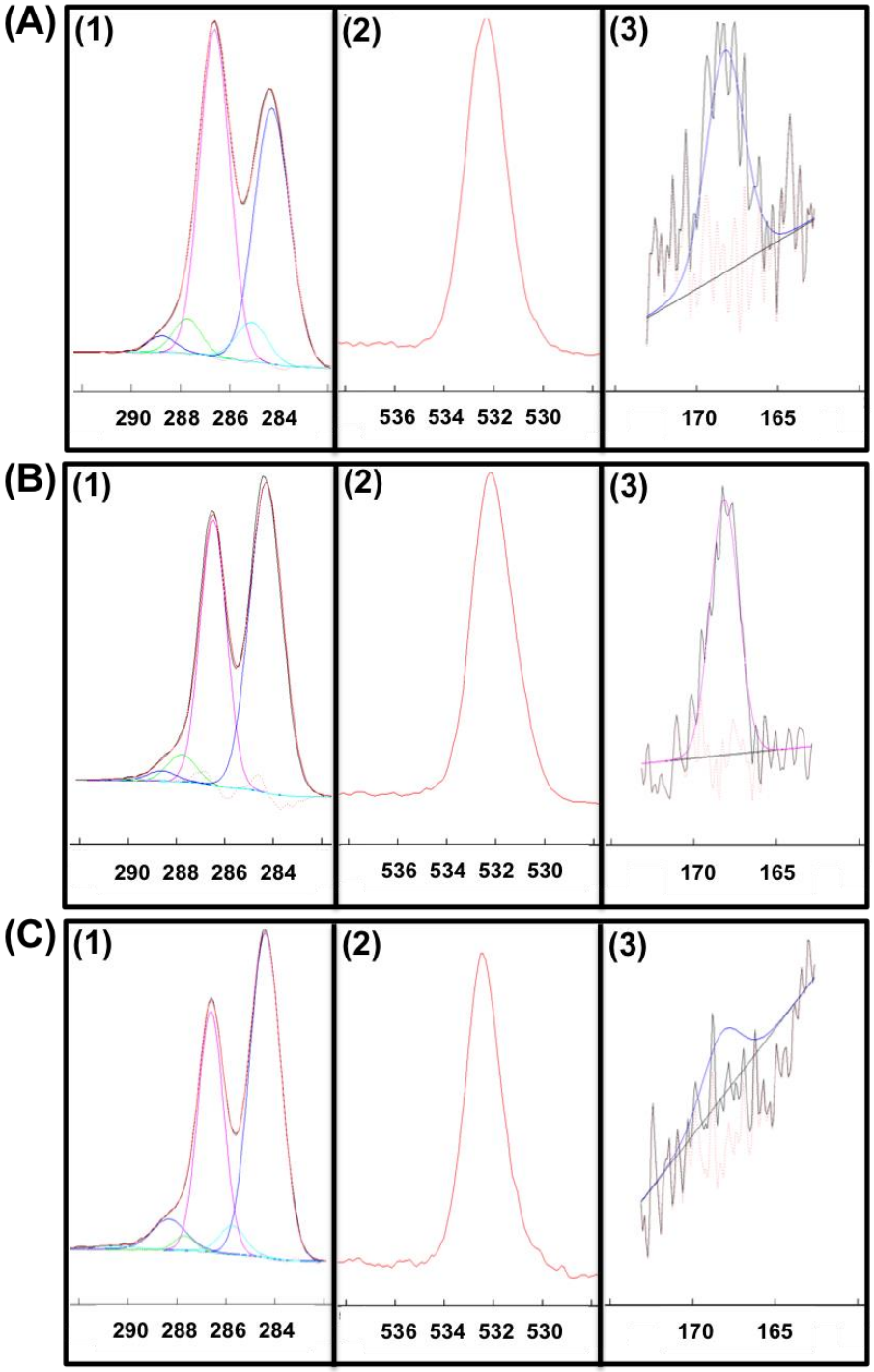

Figure 4.10 The XPS-derived intensities (a.u.) as a function of the binding energy (eV) of the (1) C 1s, (2) O 1s, and (3) S 2p regions for the GO samples: (A) **GO-23**, (B) **GO-40**, and (C) **GO-80.**

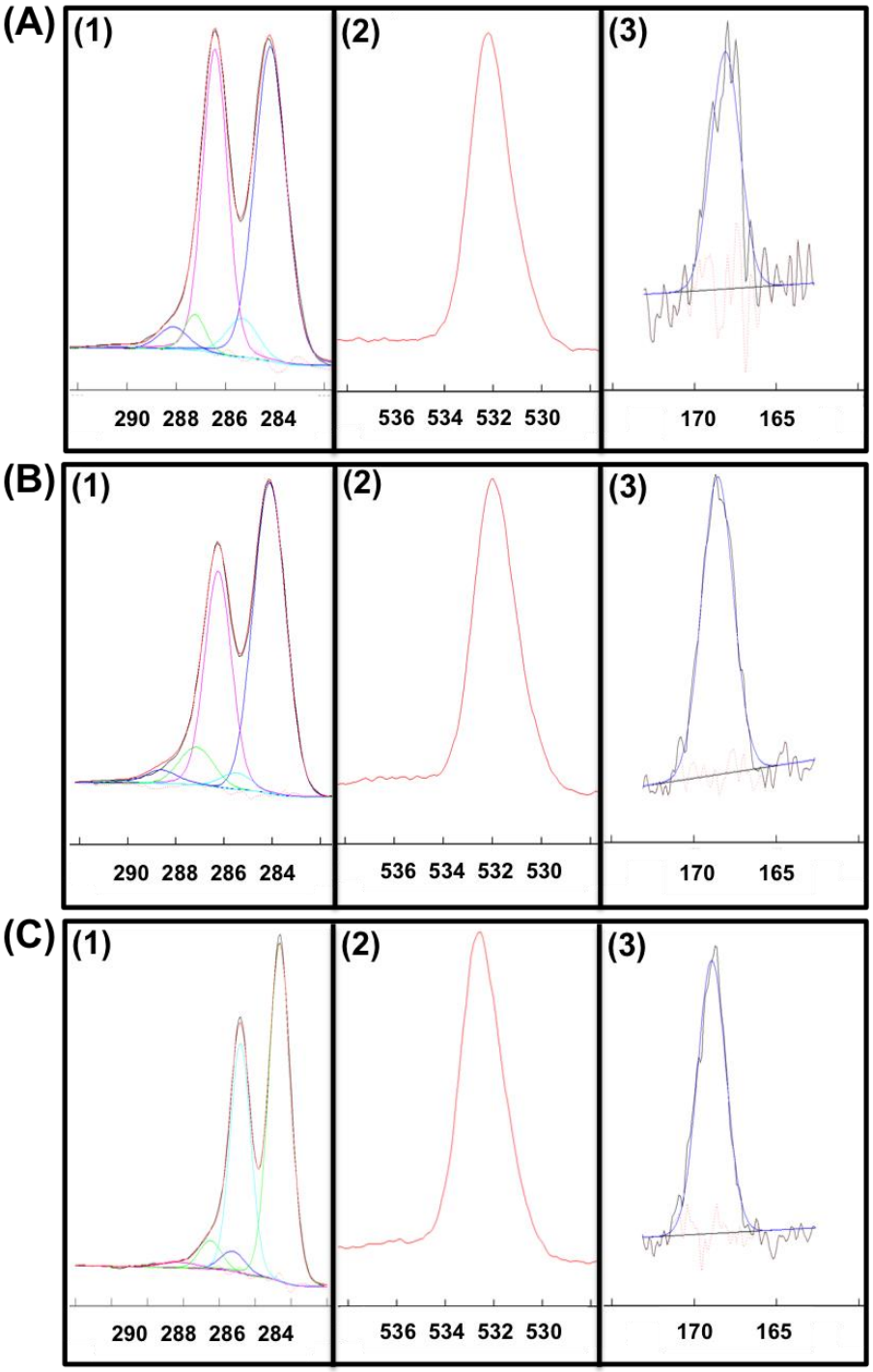

Figure 4.11 The XPS-derived intensities (a.u.) as a function of the binding energy (eV) of the (1) C 1s, (2) O 1s, and (3) S 2p regions for the sulfate modified GO samples: (A) **SS-GO-23**, (B) **SS-GO-40**, and (C) **SS-GO-80.**

C 1s Spectra. Well-defined multiple peaks were present in the C 1s BE region in the XPS data collected for all of the samples, which is consistent with a model in which the GO has been highly oxidized. The broad peak at lower binding energy (~284.5 eV) can be assigned to the framework sp^2 carbons of GO that are unoxidized, while the other broad peak at higher BE (~287 eV) represents various oxidized carbons, such as those associated with the hydroxyl, epoxy/ether, and carbonyl groups [72-77]. The various carbon species can be deconvoluted using the Multipak™ software package. The components at ~285.6, 286.7, and 287.5–289.4 eV have been previously attributed to carbons attached to the hydroxyl group (C-OH), epoxide/ether carbons (C-O-C), carbonyl carbons (>C=O), including those within the carboxyl groups, respectively, (see Table S 4.2) [72-77].

Table 4.2 Assignments of the Peaks in the C 1s Region of GO

references	graphitic sp^2 carbons	C-OH carbons	epoxy/ether carbons	carbonyl carbons
38	284.6	285.6	286.7	288.5
39	284.5	285.6	286.6	287.6
40	284.5	285.4	286.8	288.5
41	284.5	285.6	NA	289.4
42	284.5	NA	286.6	289.0
43	284.5	285.9	286.6	287.5 & 289.2

The XPS spectra for the C 1s BE region are plotted in Figure 4.10. In Figures 4.10 A-C, the set of samples that were not treated with SS exhibit a decrease in intensity for the broad peak associated with the oxidized carbons with increasing reaction

temperature, while the peak associated with the unoxidized sp^2 carbons (~284.5 eV) failed to show a similar trend. This behavior has been observed in prior studies of the hydrothermal deoxygenation of graphene oxide [78].

When epoxy groups are located in the basal plane of GO [79], they are highly strained and reactive [78]; therefore, a plausible mechanism for the chemical changes for such epoxy groups is that the rings open up, especially when the reaction temperature is increased, or SS reacts with GO. The opened epoxy groups can transform to other species, such as hydroxyl moieties [78, 80], or deoxygenation can occur. A comparison of all of the C 1s spectra in Figures 4.10 and 4.11 illustrates that the number of epoxy groups decreases as the reaction temperature increases and when SS is added as a reactant. A plotting of the intensities of the C 1s peaks (and other relevant elements) in Figure 4.12 confirms these trends, where the specific carbon assignments are based on the literature data shown in Table 4.2 [72-77].

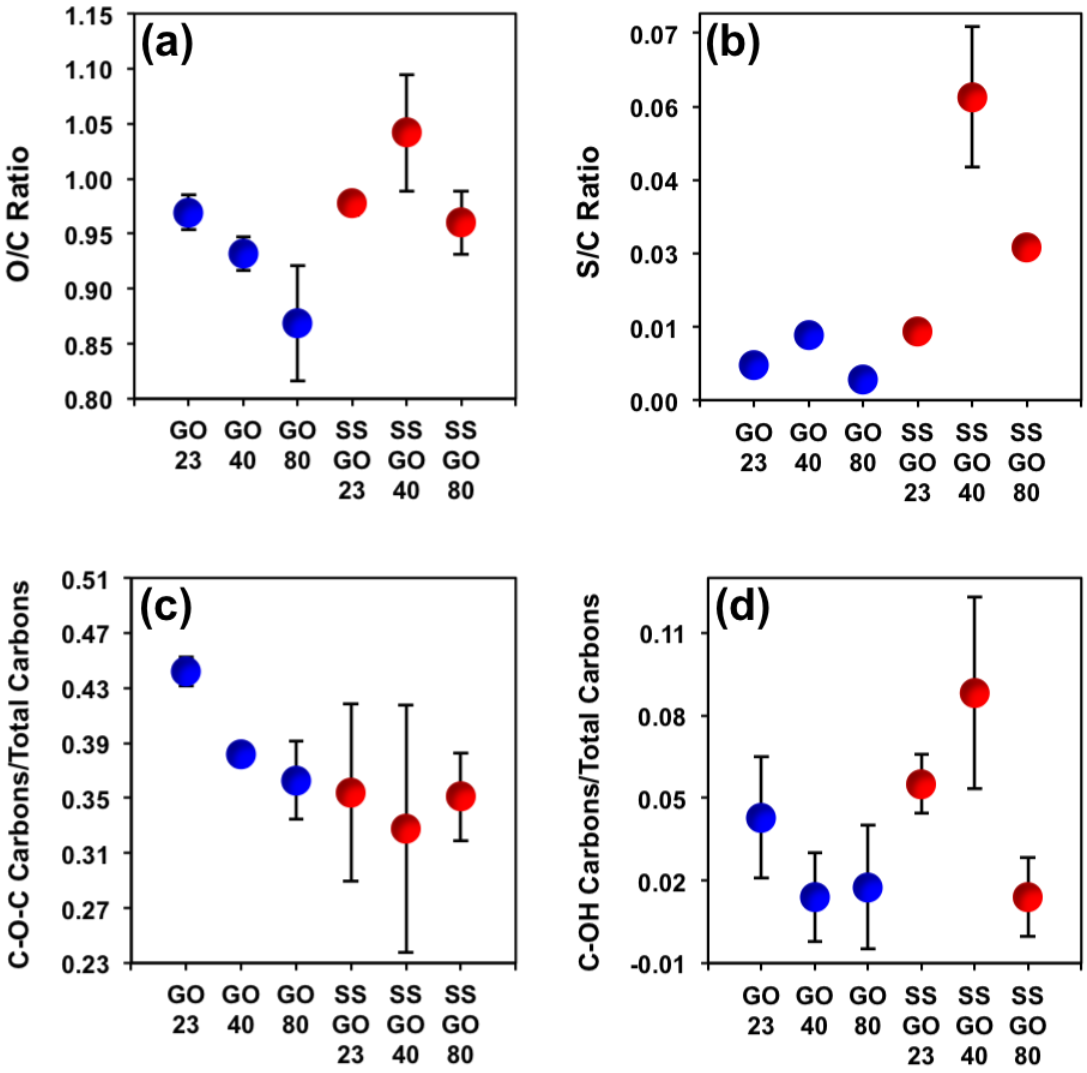

Figure 4.12 The XPS intensity ratios: (a) oxygen/carbon (b) sulfur/carbon (c) epoxy/carbon, and (d) hydroxyl/carbon. Error bars represent the standard deviation for data collected from three independent samples.

In particular, Figures 4.12c and 4.12d facilitate a comparison of the trends in the oxidized carbons (e.g., epoxy-based and hydroxyl-based) versus the unoxidized sp^2 framework carbons. Separately, Figure 4.13 shows a layered plot of the sulfur spectra to facilitate comparison of the sulfur content and species in all of the samples.

S 2p Spectra. The sulfate groups covalently attached to the GO surface showed lower binding energies of ~168 eV compared to ~170 eV for the S 2p peak of SS alone (see Figure 4.13) [81].

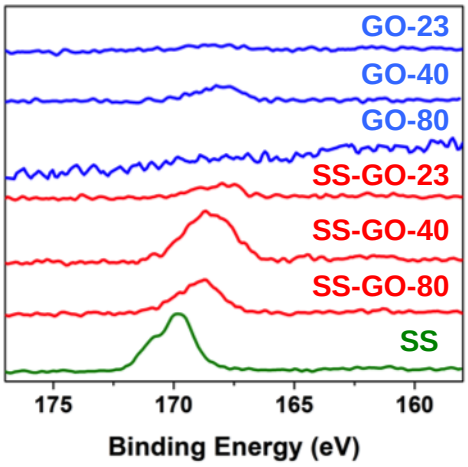

Figure 4.13 The XPS-derived intensities (a.u.) as a function of the binding energy (eV) of the S 2p regions for the all GO samples **GO-23**, **GO-40**, **GO-80**, **SS-GO-23**, **SS-GO-40**, **SS-GO-80,** and **SS.**

The amount of sulfur present after functionalization with SS at 40 ºC (**SS-GO-40**) is greater than that observed for the sample treated with SS at rt (**SS-GO-23**); however, treatment at 80 °C grafted the least amount of sulfur overall (**SS-GO-80**). This phenomenon likely arises from the ready detachment of sulfate from GO at elevated temperatures in aqueous solution. We explore this possibility through an additional experiment outlined in the following paragraph.

It is known that the O-S bond from RO-SO_3^- can be cleaved at temperatures ranging from 70 to 100 ºC, depending on the nature of the alkyl substituent [70]. Correspondingly, it appears that the O-S bond in our study is also broken at temperatures in the range of 40 to 80 ºC, which leads to more sulfate being covalently bound to the GO

after the 40 ºC reaction than after the 80 ºC reaction. To shed more light on these results, we redispersed the samples **SS-GO-23**, **SS-GO-40**, and **SS-GO-80** in Milli-Q water (0.1 mg/mL) and exposed to each respective sample to temperatures of 23, 40, and 80 ºC for 48 h and then washed with Milli-Q water 5 times. As shown in Table 4.3, the amount of sulfur present decreased by 18% and 89% for **SS-GO-23** and **SS-GO-40**, respectively; however, all the sulfur for the **SS-GO-80** sample was completely gone after reheating and washing. Notably, there was excess SS in the aqueous solution during the initial reaction to covalently attach the sulfate to GO, but no SS in the Milli-Q water when the sulfate-modified samples were re-dispersed in solution, so the equilibrium for the reaction can plausibly favor detachment, assuming the reaction is reversible. Consistent with this interpretation, the data in Table 4.3 show that the 80 ºC reaction conditions cause all of the sulfate groups to detach from GO when there is no SS in solution. Therefore, for the GO that reacted with SS at 40 ºC, the conditions are more favorable to retain the sulfate compared to the GO exposed to SS at 80 ºC.

Table 4.3 S/C Ratios for SS-Modified GO Samples before and after Re-Exposure to the Original Reaction Conditions

sample abbreviation	after sulfate modification	after re-exposure and washing
SS-GO-23	0.010	0.008
SS-GO-40	0.058	0.006
SS-GO-80	0.027	0.000

O 1s Spectra. The oxygen-to-carbon ratios were calculated from the XPS peak intensities in Figures 4.10 and 4.11 for all of the carbon species (i.e., those at ~285.6, 286.7, and

287.5–289.4 eV). The O/C ratios in Figure 4.12A for the untreated samples show a decrease from that of **GO-23** when the samples had been heated at 40 ºC and show an even greater decrease upon heating at 80 ºC due to the hydrothermal deoxygenating process. These ratios are 97%, 93%, and 87% for **GO-23**, **GO-40**, and **GO-80**, respectively. Even though the GO samples treated with SS also experience hydrothermal deoxygenation, the O/C ratios exhibit an increase relative to the comparable samples that were not treated with SS due to the attachment of sulfate moieties, which contain oxygen.

4.3.2.3 Conclusion from XPS Data

The relative counts for the oxidized carbons when compared to the framework carbons (sp^2) of GO decreased as the reaction temperature increased from 23 to 40 and then to 80 °C. For **SS-GO-23**, **SS-GO-40**, and **SS-GO-80**, compared to **GO-23**, the plots in Figure S7 show that the O/C ratio decreased by 0%, 4%, and 7% for 23 °C, 40 °C, and 80 °C, respectively; furthermore, the plots in Figure 4.12B show that the S/C ratio increased 3×, 18×, and 8×, respectively.

4.3.3 Structural Characterization Using Raman Spectroscopy

4.3.3.1 Instruments and Condition: Raman Spectroscopy

The samples were placed on top of thin glass surfaces for the Raman measurements. A 532 nm laser with a pump power of 0.2 W (Spectra Physics, Millennia Xs) was used. The beam was initially expanded and then focused onto the sample of an inverted microscope (Olympus IX71) through an epi-Raman 60× objective lens. The data were collected over a sample area of ~1.5 μm^2 (FWHM of the beam is ~1.5 μm). The scattered Raman light from the sample was filtered using a long pass filter (Semrock)

and collected by a spectrograph (Acton 300i) and CCD (Princeton 400BR). Each sample was measured for 60 s acquisition times and averaged over two frames (total acquisition time = 120 s). Data were collected for three different random spots for each sample.

4.3.3.2 Caracterization of Samples by Raman

Characterization of graphene by Raman spectroscopy reveals various structural details, such as crystalline order [82, 83] and average crystal size [68, 84, 85]. Moreover, this technique is non-destructive with rapid data collection. Raman spectroscopy has also been used to monitor doping, defects, strain, and chemical functionalization of graphene [86-88]. There is a unique resonance Raman effect from the coupling of the excitation light with a particular interband transition in graphene. However, in the case of ideal defect-free graphene, there is no resonance effect, so the peak intensity ratio (I_D/I_G) in the Raman spectrum is a simple way to interpret the relative disorder of the structure [88]. The two most significant bands in the Raman spectrum for graphitic materials are identified as the D and G bands, and these characteristic peaks can reveal how the different reaction temperatures, and the addition of SS, affect GO structurally. The G band originates from in-plain vibrations of the sp^2 carbons and is generally observed at ~1575 cm^{-1}. The D band is also in-plane and is active and typically observed at ~1350 cm^{-1} [89].

In the Raman spectra of graphene and its derivatives, the ratio of I_D/I_G provides useful information regarding whether the framework of graphene has been modified by the attachment or detachment of molecules. It has been shown that an increase I_D/I_G is due either to deoxygenation of GO or to the presence of covalently attached materials to

GO [63]. The observation of a strong D band in graphene-based samples suggests that the structure has a large number of defects and disorder [53].

In this study, we observed an increase in the I_D/I_G ratio when the GO was treated at high temperatures in aqueous solution and an even greater increase when the GO was treated at high temperatures in the presence of SS (see Figure 4.14).

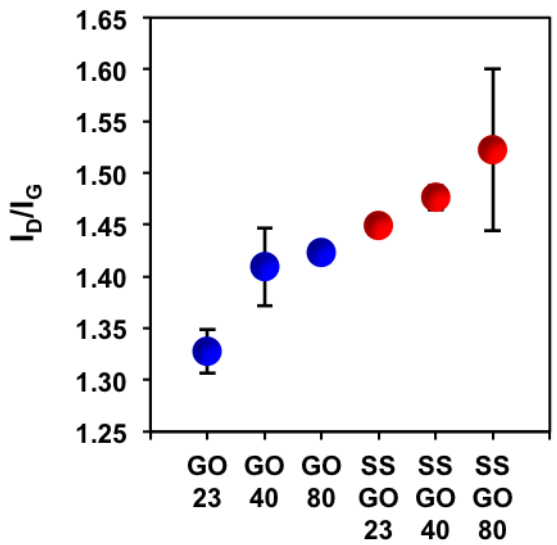

Figure 4.14 I_D/I_G data obtained from the Raman spectra of the samples. Error bars that are not visible fall within the symbols. The error bars represent the standard deviation for data collected from three independent samples

The I_D/I_G ratio increased in the order of **GO-23**, **GO-40**, and **GO-80**, a result consistent with the XPS data from the hydrothermal deoxygenation (see Figure 4.12A). As expected, the oxidized carbon ratio decreased with an increase in the reaction temperature, consistent with the observed I_D/I_G ratio obtained by Raman spectroscopy. Furthermore, the GO samples that were exposed to SS (**SS-GO-23**, **SS-GO-40**, and **SS-GO-80**) have more defects than the GO samples that were not exposed to SS under the same thermal conditions due to the sulfate moieties covalently bonding to GO [71]. The

I_D/I_G data indicate further that the **SS-GO-80** samples have more defects than the other samples, even though the number of sulfate groups attached is less than that for the **SS-GO-40** samples, because the SS moiety has a greater likelihood of being detached at temperatures above 40 °C [90]. In other words, while more SS moieties can become attached at 80 °C, the reverse reaction is also facile at that temperature, leaving more defects on **SS-GO-80**; this model is supported by the results shown in Table 4.3 in the Supporting Information. In short, the **SS-GO-80** samples have more defects than the other samples, but also have less attached sulfate moieties. This model is also consistent with the observation that the **SS-GO-80** samples have the lowest Ms (see Figure 4.2A); notably, the magnetization arises from a combination of attached sulfate species and the presence of various types of defects (e.g., defects caused by the process of sulfate attachment/detachment and hydrothermal deoxygenation). In summary, the deoxygenation of GO and sulfate grafting to GO leads to an enhanced number of sp^2 carbon domains, but with smaller sizes, which increases the I_D/I_G ratio [71].

4.3.4 Functional Group Characterization Using Infrared Spectroscopy

4.3.4.1 Instruments and Conditions: Infrared (IR) Spectroscopy

IR spectra were recorded from powder samples on a Thermo Scientific Nicolet IS5 infrared spectrometer. The spectral data were acquired using 48 scans at a resolution of 4 cm^{-1}.

4.3.4.2 Characterization of Samples by IR

Infrared absorption spectroscopy is an important tool for unraveling the chemical composition of samples. The presence of specific chemical bonds typically associated with certain functional groups can be determined from the wavenumber, shape, and width of the peaks in the IR spectra, providing qualitative and, with limitations, quantitative data. Characteristic peaks shift higher (blue shifts) or lower (red shifts) and broaden or sharpen in response to the local environment and are further influenced by π conjugation [71].

The six peaks shown in Figure 6 associated with readily identified structural features for these samples are centered at ~3400, 1730, 1620, 1385, 1217, and 1045 cm^{-1}, which can be assigned to the hydroxyl O–H bond, the C=O bond from COOH, the aromatic C=C bonds from skeletal vibrations of sections of sp^2 framework of GO, the C–OH bond from COOH, the C–O bond from epoxy rings, and the C–O bond from hydroxyl stretching vibrations, respectively [55, 71, 90]. For the SS spectrum, the most significant peak located at 1083 cm^{-1} arises from the S=O bond of sulfate.

There are a few significant changes between the GO samples treated with SS compared to the samples not treated with SS. The most significant observation is that the samples exposed to heating are more deoxygenated with increasing reaction temperature (especially 80 ºC), which is consistent with the XPS and Raman data. This effect can be attributed to hydrothermal deoxygenation [55]. The O-H stretching associated with the hydroxyl group (~3400 cm^{-1}) shows the greatest reductions (see, for example, the spectra for the **GO-80** and **SS-GO-80** samples in Figures 4.15C and 4.15F, respectively). Also, the peaks attributed to the C–O (1385 cm^{-1}) and C=O (~1730 cm^{-1}) bonds from COOH

are significantly diminished for the samples treated at 80 ºC. The peak for the C–O bond for the carboxylic acid groups, which is located at ~1370 cm^{-1} for **GO-23**, exhibits a blue shift to ~1410 cm^{-1} for the **GO-80** and **SS-GO-80** samples, perhaps due to the reduction in nearby hydroxyl groups as described above [71]. The peak at ~1580 cm^{-1} can be assigned to the sp^2-hybridized C=C backbone in GO, while the peak at ~1600 cm^{-1} arises from an oxidized graphene framework [92,93]. Therefore, the IR spectra of the samples treated at 80 ºC, **GO-80** and **SS-GO-80**, exhibit a red shift from ~1626 to ~1585 cm^{-1} upon heating above 40 °C [92, 93].

With regard to an analysis of the sulfate-based peaks in the SS-modified samples, the spectra show no obvious peak at 1083 cm^{-1} nor any additional peaks at 950~1300 cm^{-1}, which are characteristic of organic sulfates (for which the S–O ν_{as} band appears at 1200 and 1300 cm^{-1}, and the S–O ν_s band appears at 950 and 1100 cm^{-1}) [94]. Our inability to observe these peaks can be attributed to (1) the low concentration of sulfate species in the samples and (2) overlapping peak intensities over this range of frequencies due to functional group contributions from various C–O stretching modes (e.g., hydroxyl and epoxy/ether).

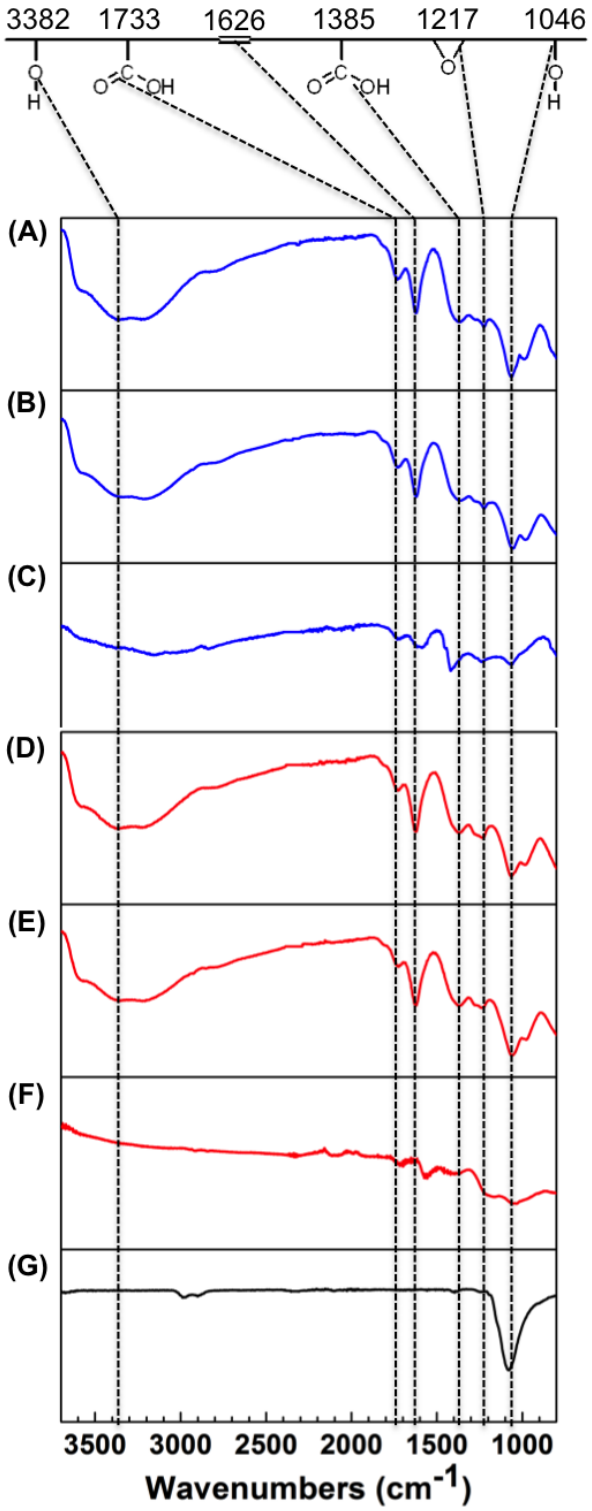

Figure 4.15 IR spectra of graphene oxide samples prepared under various reaction conditions along with a spectrum of sodium sulfate: (A) **GO-23**, (B) **GO-40**, (C) **GO-80**, (D) **SS-GO-23**, (E) **SS-GO-40**, (F) **SS-GO-80**, and (G) **SS.**

4.3.5 Acid/Base Stability/Dipersibility Test

We performed stability/dispersibility tests to verify that the sulfate groups were covalently attached to the GO. Prior reports have noted that GO is dispersible in an aqueous phase due to the presence of carboxylic acid groups that readily ionize to form carboxylate (COO^-) groups [95]. The GO sheets can be stably dispersed above a pH value of ~4, with some variance in the exact pH value depending on the chemical environment near the carboxylic acid moieties (e.g., functional groups that are present and the proximity of these functional groups to each other) [96]. Another important consideration is that these moieties typically populate the edges of GO [95]. Therefore, GO samples tend to aggregate and then precipitate in aqueous solution as the pH drops below a value of ~4 since the $–COO^–$ anions are protonated and become –COOH, enabling the formation of hydrogen bonds between GO flakes. However, the sulfate-functionalized GO are less likely to aggregate under these conditions because the surface-bound sulfate group has a lower pK_a value than the graphene-bound carboxylate group [66]. Therefore, we anticipated that the sulfate-functionalized GO samples would exhibit enhanced stability under acidic conditions. With this knowledge to support our efforts, we conducted tests on all of the GO samples at varying pH conditions. Selected pH solutions were prepared with NaOH and HCl at concentrations ranging from 2×10^{-6} M to 2×10^{-1} M, and then 1 mL of each of these solutions was mixed with 1 mL of each of the six samples. Figure 4.16 shows the data obtained over the range of 10^{-1} M NaOH to 1 M HCl.

As shown in Figures 4.16A, 4.16C, and 4.16E, the GO samples untreated with SS (**GO-23**, **GO-40**, and **GO-80**) started to aggregate and then precipitate in each of the

solutions prepared by adding 1 mL of 2×10^{-2} or 2×10^{-1} M HCl to the GO solution. In contrast, the sulfate-functionalized GO samples (**SS-GO-23**, **SS-GO-40**, and **SS-GO-80**) were still well dispersed in solution at the lower pH values, including the samples that had been exposed to elevated temperatures. However, for the most acidic conditions, those samples also started to aggregate, as shown in Figures 4.16B, 4.16D, and 4.16F.

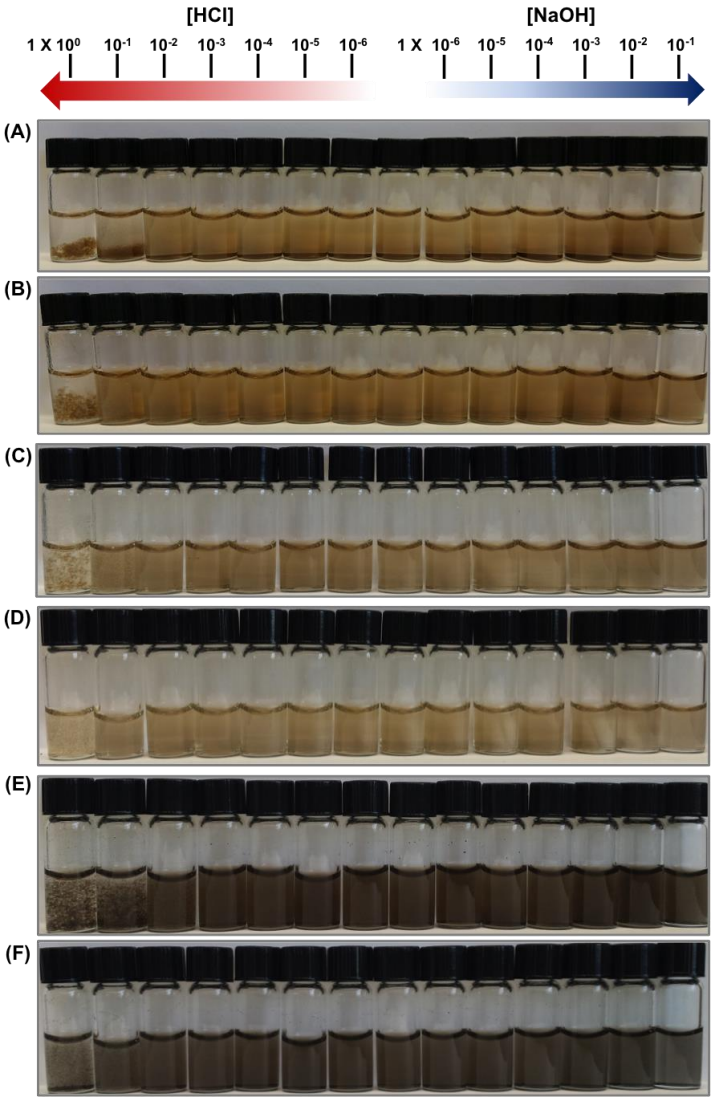

Figure 4.16 Photographs of a series of solutions of graphene oxide further exposed to various pH conditions using either HCl or NaOH: (A) **GO-23**, (B) **SS-GO-23**, (C) **GO-40**, (D) **SS-GO-40**, (E) **GO-80**, and (F) **SS-GO-80.**

4.4 Conclusions

This report described a novel, simple, and accessible technique for the functionalization of graphene oxide by means of moderate thermal treatment with sodium sulfate. Such modification altered the electronic structure of GO and led to the formation of frustrated magnetic phases, where magnetic defects and localized spins were coupled through RKKY interactions. From the results, we can conclude that SS functionalization played a critical role in enabling the long range RKKY coupling between the magnetic impurities in graphene oxide. The emergence of a frustrated magnetic phase was supported by a systematic increase in the saturation magnetization and finite coercivity observed at room temperature. The random distribution of structural defects naturally abundant in GO, localized electronic states, and oscillatory nature of long range RKKY interaction allowed us to propose that the observed magnetic phase exhibited a spin-glass nature. Our proposal was further supported by the observation of irreversibility in the ZFC-FC curves obtained at 100 Oe and 1 T. According to the results in this paper along with recent reports from other researchers, we conclude that structural defects, bound oxygen, and sulfate-functionalization enabled an enhancement of the magnetic properties of graphene oxide. Our research paves that way for further exploration of the capacity of electron-withdrawing/donating groups and structural defects in conjugated carbon nanosystems for tuning their magnetic and electronic properties.

Chapter 5. Summary and Future Work

The areal density for magnetic hard drives can be increased by decreasing the size of the magnetic bits or reducing the numbers of grains per bit. However, both approaches are challenging because miniaturization leads to data stability issues due to the superparamagnetic limit and the case of fewer grains per bit is less reliable. The approach with having one grain per bit is promising because a larger volume of magnetic material improves both stability and readability.

Bit-patterned media (BPM) is comprised of a well ordered distinct array of patterned with magnetic materials, so such that each of the isolated material serve as one bit. The patterned media can be fabricated with higher areal density by Ar^+ milling. BPM technology can enable areal densities beyond 1 Tb/in^2. Traditional methods for nanopattern fabrication such as electron beam lithography suffer from a variety of limitations: time consuming, expensive, dimensions less than 100 nm with fine corners is difficult to achieve. Therefore, self-assembled block copolymer (BCP) patterns provide a viable alternative strategy. The BCP patterns are naturally circular because such geometry is thermodynamically favorable for a system of two polymers. Noncircular magnetic device patterns offer some advantages over circular device patterns such as increased thermal stability and signal to noise ratio.

This dissertation describes the fabrication and manipulation of polymeric materials to produce nanoscale devices. Hexagonal BCP patterns were demonstrated by processing polystyrene-block-polymethyl methacrylate (PS-b-PMMA) BCP thin films.

For future work, the patterned thin film can be used as a mask or filled with magnetic materials to form BPM.

As one of potential materials for the data storage applications, graphene has received significant interest from the research community. However, little is known about graphene's magnetic properties although it's extraordinary conductivity, mechanical, thermal, and optical properties have been studied extensively. The study of magnetism in 2D nanomaterial such as graphene and/or its derivatives present particularly large challenges due to the complexity of the system such as structural defects and the effects of the boundaries as well as chemical functionalization. Experimental investigation plays the crucial role in understanding the magnetic properties of graphene and its derivatives. We examine the properties of the flakes of GO before and after their "chemical modification" by sodium sulfate in order to systemically investigate its effect on the magnetic properties of the material.

From our investigation, we conclude that the combination of defects, oxygen and sulfate group, play a major role in the emergence of magnetism in GO. It is essential to understand and develop the ability to tune the magnetic properties to pursue prospective applications of graphene-based materials in nanomagnetoelectronics, spintronics, and magnetic memory devices. The magnetic force microscopy (MFM) or spin-polarized/scanning tunneling microscopy (SP/-STM) can be used to observe the density of electron states and their spin states in situ. This work provides new insight on the room temperature magnetic properties of organic molecules and a basis for further experimental and theoretical investigations.

References

1. Munce, A. C.; Thiele, J.-U. *Hitachi Reviews* **2006**, 55, 150–154.
2. Retrieved from www.seagate.com (accessed July 1, 2016).
3. Wood, R. *Journal of Magnetism and Magnetic Materials* **2009**, *321*, 6, 555–561.
4. Litvinov, D.; Khizroev, S. *Proceedings of the 10th NASA Goddard Space Flight Center Conference on Mass Data Storage systems and Technologies* **2002**, 1–19.
5. Ed, G. Longitudinal and Perpendicular recording Schematics. *Hitachi Global Storage Services.* **2005**.
6. Mallary M.; Torabi A.; Benakli M. *IEEE Transactions on Magnetics* **2002**, *38*, 1719–1724.
7. Bertram, H. N.; Williams, M. *IEEE Transactions on Magnetics* **2000**, *36*, 49.
8. Charp, S. H.; Lu, P.-L.; He, Y. *IEEE Transaction on Magnetic* **1997**, *33*, 1.
9. Ross, C. *Annual Review of Materials Research* **2001**, *31*, 203–235.
10. Rottmayer, R. E.; Batra, S.; Buechel, D.; Challener, W. A.; Hohlfeld, J.; Kubota, Y.; Li, L.; Lu, B.; Mihalcea, C.; Mountfield, K.; Pelhos, K.; Peng, C.; Rausch, T.; Seigler, M. A.; Weller, D.; Yang, X. –M. *Magnetics, IEEE Transactions on Magnetics* **2006**, *42*, 2417–2421.
11. McDaniel, T. W.; Challener, W. A.; Sendur, K. *IEEE Transactions on Magnetics* **2003**, *39*, 1972–1979
12. McDaniel, T. W. *Journal of Physics Condensed Matter* **2005**, *17*, 315–332.
13. Wood, R.; Williams, M.; Kavcic, A.; Miles, J. *IEEE Transactions on Magnetics* **2009**, *45*, 917–923.
14. Gavrila, H. *Journal of Optoelectronics and Advanced Materials* **2004**, *6*, 891–903.
15. Terris, B. D.; Thomson, T.; Hu, G. *Microsystem Technologies* **2007**, *13*, 189–196.
16. Munce, A. C.; Thiele J. *Hitachi Review* **200**6, *55*, 150–154.
17. Wolf, S. A.; Awschalom, D. D.; Buhrman, R. A.; Daughton, J. M.; von Molnar, S.; Roukes, M. L.; Chtchelkanova, A. Y.; Treger, D. M. *Science* **2001**, *294*, 1488–1495.
18. Wang, W. L.; Meng. S.; Kaxiras, E. *Nano Lett* **2008**, *8*, 241–245.

19. Yazyev, O. V. *Nano Lett* **2008**, *8*, 1011–1015.
20. Fischer, J.; Trauzettel, B.; Loss, D. *Phys. Rev. B* **2009**, *80*, 155401.
21. Lin, A. L.; Peng, H.; Liu. Z.; Wu, T.; Su, C.; Loh, K. P.; Ariando.; Chen, W.; Wee, A. T. S. *Small* **2014,** *10*, 1945–1952.
22. Trauzettel, B.; Bulaev, D. V.; Loss, D.; Burkard, G. *Nat. Phys* **2007**, *3*, 192–196.
23. Yazyev, O. V. *Rep. Prog. Phys*. **2001**, *73*, 056501.
24. Awschalom, D. D.; Flatté, M. E. *Nature. Phys* **2007**, *3*, 153–159.
25. Chappert, C.; Fert, A.; Van Dau, F. N. *Nat. Mater.* **2007**, *6*, 813–823.
26. Parekh, A. V.; Ruiz, A.; Ruchhoeft, P.; Brankovic, S.; Litvinov, D. *Nano Lett.* **2007**, *7*, 3246–3248.
27. Marcon, V.; Vegt, N. F. A. *Soft Matter* **2014**, *10*, 9059.
28. Nanofabrication Facility at the University of Houston http://www.nanofab.uh.edu/equipment/pattern-making/ebeam-writer
29. Ma, S.; Con, C.; Yavuz, M.; Cui, B. *Nanoscale Research Letters* **2011**, *6*, 446.
30. Thompson, L. F.; Kerwin, R. E. *Annu. Rev. Mater. Sci.* **1976,** *6*, 267–230.
31. Ku, H. Y.; Scala, L. C. *J. Electrochem. Soc.* **1969**, *116*, 980–985.
32. Con, C.; Dey, R.; Ferguson, M.; Zhang, J.; Mansour, R.; Yavuz, M.; Cui, B. *Microelectronic Engineering* **2012**, *98*, 254.
33. Atoda, N,; Kawakatsu, H. *J. Electrochem. Soc.: Solid State Sci. Technol.* **1976**, *123*, 1519.
34. Sugita, K.; Ueno, N. *Prog. Polym. Sci*. **1992**, *17*, 319.
35. Dey, R. K.; Cui, D. B. *Nanotechnology* **2013**, *24*, 245302.
36. Austin, M. D.; Zhang W.; Ge, H.; Wasserman, D.; Lyon, S. A.; Chou, S. Y. *Nanotechnology* **2005**, *16*, 1058–1061.
37. Ahn, D.; Erol, S. *Soft Matter* **2008**, *4*, 1454–1466.
38. Dolan J. A.; Wilts B. D.; Vignolini S.; Baumberg J. J.; Steiner U.; Wilkinson T. D. *Adv. Optical Mater*. **2015**, *3*, 12–32.
39. Kim H.-C.; Park S. -M.; Hinsberg W. D. *Chem. Rev.* **2010**, *110*, 146–177.
40. Vu T.; Mahadevapuram N.; Perera G. M.; Stein G. *Macromolecules* **2011**, *44*, 6121–6127.

41. Shakarisaz, D. **2016**. Stencil Mask Development for Atom Beam Proximity Lithography and Engineered Nanoparticle Fabrication (unpublished doctoral dissertation). University of Houston, Houston, Texas, USA.
42. Tuinstra, F.; Koenig, J. L. Raman Spectrum of Graphite. *J. Chem. Phys.* **1970,** *53*, 1126–1130.
43. Niyogi, S.; Bekyarova, E.; Itkis, M. E.; Zhang, H.; Shepperd, K.; Hicks, J.; Michael, S.; Berger, C.; Lau, C. N.; deHeer, W. A.; Conrad, E. H.; Haddon, R. C. *Nano Lett* **2010**, *10*, 4061–4066.
44. Gomez-Navarro, C.; Burghard, M.; Kern, K. *Nano Lett* **2008**, *8*, 2045–2049.
45. Balandin, A. A. *Nat. Mater. Rev.* **2011**, *10*, 569–581.
46. Bonaccorso, F.; Sun, Z.; Hasan, T.; Ferrar, A. C. *Nature Photon* **2010**, *4*, 611–622.
47. Wang, Z.; Eigler, S.; Ishii, Y.; Hy, Y.; Papp. C.; Lytken, O.; Steinrück, H.-P.; Halik, M. A. *J. Mater. Chem. C* **2015**, *3*, 8595–8604.
48. Hong, A. J.; Song, E. B.; Yu, H. S.; Allen, M. J.; Kim, J.; Fowler, J. D.; Wassei, J. K.; Park, Y.; Wang, Y.; Zou, J.; Kaner, R. B.; Weiller, B. H.; Wang, K. L. *ACS Nano* **2011,** *5*, 7812–7817.
49. Li, W.; Zhao, M.; Xia, Y.; Zhang, R.; Mu, Y. *J. Mater. Chem.* **2009**, *19*, 9274–9282.
50. Alexander, S. S.; Lucio, A. D.; Neto, A. H. C.; Nunes, R. W. *Nano Lett* **2012**, *12*, 5097–5102.
51. Yazyev, O. V.; Helm, L. *Phys. Rev. B* **2007**, *75*, 125408.
52. Wang, W. L.; Yazyev, O. V.; Meng, S.; Kaxiras, E. *Phys. Rev. Lett.* **2009**, *102*, 157201.
53. López-Sancho, M. P.; de Juan, F.; Vozmediano, M. A. H. *Phys. Rev. B* **2009**, *79*, 075413.
54. Boukhvalov, D. W.; Katsnelson, M. I. *Nano Lett* **2008**, *8*, 4373–4379.
55. Sarkar, S. K.; Raul, K. K.; Pradhan, S. S.; Basu, S.; Nayak, A. *Physica E* **2014**, *64*, 78–82.
56. Sun, P.; Wang, K.; Wei, J.; Zhong, M.; Wu, D.; Zhu, H. *Nano Research* **2014**, *7*, 1507–1518.

57. Chua, C.; Pymera. M. *Chem. Soc. Rev*. **2013**, *42*, 3222–3233.
58. Bekyarova, E.; Itkis, M. E.; Ramesh. P.; Berger, C.; Sprinkle, M.; De Heer, W. A.; Haddon, R. C. *J. Am. Chem. Soc.* **2009**, *131*, 1336–1337.
59. Hong, J.; Niyogi, S.; Bekyarova, E.; Itkis, M. E.; Ramesh, P.; Amos, N.; Litvinov, D.; Berger, C.; de Heer, W. A.; Khizroev, S.; Haddon, R. C. *Small* **2011**, *7*, 1175–1180.
60. Hong, J.; Bekyarova, E.; de Heer, W. A.; Haddon, R. C.; Khizroev, S. *ACS Nano* **2013**, *7*, 10011–10022.
61. Englert, J. M.; Dotzer, C.; Yang, G.; Schmid, M.; Papp, C.; Gottfried, J. M.; Steinrück, H.-P.; Spiecker, E.; Hauke, F.; Hirsch, A. *Nat. Chem.* **2011**, *3*, 279–286.
62. Chua, C. K.; Pumera, M. *ACS Nano* **2015**, *9*, 4193–4199.
63. Khurana, G.; Kumar, N.; Kotnala, R. K.; Nautiyal T.; Katiyar, R. S. *Nanoscale* **2013**, *5*, 3346–3351.
64. Nair, R. R. *et al. Nat. Phys.* **2012**, *8*, 199–202.
65. Matte, H. S. S. R.; Subrahmanyam, K. S.; Rao, C. N. R. *J. Phys. Chem. C* **2009**, *113*, 9982–9985.
66. Ganguly, A., Sharma, S., Papakonstantinou, P., Hamilton, J. *J. Phys. Chem C* **2011**, *115*, 17009–17019.
67. Power, S. R.; Ferreira, M. S. *Crystals* **2013**, *3*, 49–78.
68. Ruderman M. A.; Kittel C. *Phys. Rev*. **1954**, *96*, 99–102.
69. Liu, J., Xue, Y., Dai, L. *J. Phys. Chem. Lett.* **2012**, *3*, 1928–1933.
70. Lee, C.-L.; Wan, C.-C.; Wang, Y.-Y. *Adv. Funct. Mater.* **2001**, *11*, 344–347.
71. Acik, M.; Lee, G.; Mattevi, C.; Pirkle, A.; Wallace, R. M.; Chhowalla, M.; Cho, K.; Chabal, Y. *J. Phys. Chem. C* **2011**, *115*, 19761–19781.
72. Yang, H.; Li, F.; Shan, C.; Han, D.; Zhang, Q.; Niu, L.; Ivaska, A. *J. Mater. Chem*. **2009**, *19*, 4632–4638.
73. Byun, I.-S.; Kim, W.; Boukhvalov, D. W.; Hwang, I.; Son, W. S.; Oh, G.; Choi, J. S.; Yoon, D.; Cheong, H.; Bail, J.; Shin, H.-J.; Shiu, H. W.; Chen, C.-H.; Son, Y.-W.; Park, B. H. *NPG Asia Materials* **2014**, *6*, 1–6.
74. Wang, P.; Zhai, Y.; Wang, D.; Dong, S. Nanoscale **2011**, *3*, 1640–1645.

75. Compton, O.; Jain, B.; Dikin, D. A.; Abouimrane, A.; Amine, K. Nguyen, S. *ACS Nano* **2011**, *5*, 4380–4391.
76. Chen, J.; Liu, S.; Feng, W.; Zhang, G.; Yang, F. *Phys. Chem. Chem. Phys*. **2013**, *15*, 5664–5669.
77. Chen, D.; Feng, H.; Li, J. *Chem. Rev.* **2012**, *112*, 6027–6053.
78. Mungse, H. P.; Sharma, O. P.; Sugimura, H.; Khatri, O. P. *RSC Adv*. **2014**, *4*, 22589–22595.
79. Dreyer, D. R.; Park, S.; Bielawski, C. W.; Ruoff, R. S. *Chem. Soc. Rev.* **2010**, *39*, 228–240.
80. Dimiev, A.; Kosynkin, D. V.; Alemany, L. B.;Chaguine, P.; Tour, J. M. *J. Am. Chem. Soc.* **2012**, *134*, 2815–2822.
81. Zhou, G.; Paek, E.; Hwang, G. S.; Manthiram, A. *Nat. Commun.* **2015**, *6*, 7760.
82. Cancado, L. G.; Jorio, A.; Martins Ferreira, E. H.; Stavale, F.; Achete, C. A.; Capaz, R. B.; Moutinho, M. V. O.; Lombardo, A.; Kulmala, T. S.; Ferrari, A. C. *Nano Lett* **2011**, *11*, 3190–3196.
83. Jorio, A.; Lucchese, M. M.; Stavale, F.; Martins Ferreira, E. H.; Moutinho, M. V. O.; Capaz, R. B.; Achete, C. A. *J. Phys. Condens. Matter* **2010**, *22*, 334204.
84. Stankovich, S.; Dikin, D. A.; Piner, R. D.; Kohlhaas, K. A.; Kleinhammes, A.; Jia, Y.; Wu, Y.; Nguyen, S. T.; Ruoff, R. S. *Carbon* **2007**, *45*, 1558–1565.
85. Park, S.; An, J.; Piner, R. D.; Jung, I.; Yang, D. X.; Velamakanni, A.; Nguyen, S. T.; Ruoff, R. S. *Chem. Mater*. **2008**, *20*, 6592–6594.
86. Pisana, S.; Lazzeri, M.; Casiraghi, C.; Novoselov, K. S.; Geim, A. K.; Ferrari, A. C.; Mauri, F. *Nat. Mater.* **2007**, *6*, 198–201.
87. Ferrari, A. C. *Solid State Commun.* **2007**, 143, 4757.
88. Sharma, R.; Baik, J. H.; Perera, C. J.; Strano, M. S. *Nano Lett* **2010**, *10*, 398–405.
89. Qin, S.; Guo, X.; Cao, Y.; Ni, Z.; Xu, Q. *Carbon* **2014**, *78*, 559–565.
90. Ogoshi, T.; Ichihara, Y.; Yamagishi, T.-A.; Nakamoto, Y. *Chem. Commun*. **2010**, *46*, 6087–6089.
91. Kim, U. J.; Furtado, C. A.; Liu, X.; Chen, G.; Eklund, P. C. *J. Am. Chem. Soc*. **2005**, *127*, 15437–15445.
92. Ciszewski, M.; Mianowski, A. *CHEMIK* **2013**, *67*, 267–274.

93. Georgakilas, V.; Otyepka, M.; Bourlinos, A. B.; Chandra, V.; Kim, N.; Kemp, K. C.; Hobza, P.; Zboril, R.; Kim, K. S. *Chem. Rev*. **2012**, *112*, 6156–6214.
94. Raza, M.; Bachinger, A.; Zahn, N.; Kickelbick, G. *Materials* **2014**, *7*, 2890–2912
95. Shih, C.-J.; Lin, S., Sharma, R.; Strano, M. S.; Blankschtein, D. *Langmuir* **2012**, *28*, 235–241.
96. Konkena, B.; Vasudevan, S. *J. Phys. Chem. Lett*. **2012**, *3*, 867–872.